PHYSICAL REVIEW RESEARCH **4**, 033248 (2022)

# Laser ion acceleration from tailored solid targets with micron-scale channels

K. V. Lezhnin[1,*] and S. V. Bulanov[2,3]
[1]Department of Astrophysical Sciences, Princeton University, Princeton, New Jersey 08544, USA
[2]Institute of Physics of the ASCR, ELI-Beamlines, Na Slovance 2, 18221 Prague, Czech Republic
[3]Kansai Photon Science Institute, National Institutes for Quantum and Radiological Science and Technology,
8-1-7 Umemidai, Kizugawa-shi, Kyoto 619-0215, Japan

(Received 17 January 2022; accepted 15 August 2022; published 29 September 2022)

Laser ion acceleration is a promising concept for the generation of fast ions using a compact laser-solid interaction setup. In this study, we theoretically investigate the feasibility of ion acceleration from the interaction of petawatt-scale laser pulses with a structured target that embodies a micron-scale channel filled with relativistically transparent plasma. Using 2D and 3D particle-in-cell (PIC) simulations and theoretical estimates, we show that it is possible to generate GeV protons with high volumetric charge and quasimonoenergetic feature in the energy spectrum. Optimal parameters of the target are obtained using 2D PIC simulations and interpreted on a basis of an analytical two-stage ion acceleration model. 3D PIC simulations and realistic preplasma profile runs with 2D PIC show the feasibility of the presented laser ion acceleration scheme for the experimental implementation at the currently available petawatt laser facilities.

DOI: 10.1103/PhysRevResearch.4.033248

## I. INTRODUCTION

While modern laser facilities have a potential of reaching ultrahigh intensities up to $10^{24}$ W/cm$^2$ [1], delivering laser fields up to 1 GV/$\mu$m, acceleration of charged particles using laser-target interaction becomes more of an interest. Highly energized charged particle beams have a broad range of applicability [2]: Imaging [3], medicine [4,5], controlled nuclear fusion [6], and nuclear physics [7]. Beams of charged particles may reach ultrarelativistic energies, with the current record of electron bunches being accelerated up to ∼10 GeV [8] using state-of-the-art Laser Wake Field Acceleration (LWFA) mechanism [9]. Ion acceleration is also estimated to be efficient from theory and simulations [10–13], but the experimental research reports the saturation of the maximum attainable ion energies on 100 MeV level [14,15]. Up and coming lasers with peak powers reaching 10 PW [16–18] may help to overcome this level of ion energies, but the need for the theoretical understanding of limiting factors still exists. Therefore, a more detailed investigation of laser ion acceleration schemes, incorporating such physics as prepulse effects [19–21], field ionization [22], oblique incidence [23], pointing stability [24], and radiation reaction effects [25], is necessary for successful experimental delivery of high-energy ion beams on a new generation of petawatt laser facilities.

On the theory side of laser ion acceleration, there are a few major mechanisms being discussed recently. The current state-of-the-art mechanism is target normal sheath acceleration (TNSA) (see [26], review articles [2,11,12,27] and references therein, and [15,28–32] for the recent experiments on TNSA), which is realized by a build-up of an electrostatic field on the rear side of the thick target due to abundance of hot electrons generated by a laser interacting with the front of the target. Accelerating electric field is known to be proportional to $(T_{\mathrm{e,nth}} n_{\mathrm{e,nth}})^{1/2}$, with $T_{\mathrm{e,nth}}$ and $n_{\mathrm{e,nth}}$ denoting hot electron temperature and density, respectively, and multiple efforts are made in order to increase both hot electron population properties [15,33–37]. A very promising maximum ion energy scaling with laser pulse power is provided by radiation pressure acceleration (RPA) [38–40], which was observed experimentally [14,22,41–46]. Multiple other mechanisms are also discussed, such as relativistically induced transparency acceleration (RITA) [47–49], Coulomb explosion [50], magnetic vortex acceleration (MVA) [51–54], collisionless shock acceleration (CSA) [55], and combinations of these [56–59].

Recently, solid-state targets started to gain more interest for electron acceleration [60,61], ion acceleration [33,34,37], and the development of radiation sources, such as x-ray [62,63] and $\gamma$-ray [64,65]. In principle, higher density targets may lead to higher densities of fast electrons [34,37] and better retention of fast electrons around laser-solid interaction spot [66], which should benefit such acceleration schemes as TNSA and MVA. On the other hand, solid densities are generally opaque for optical laser pulses, which suppresses laser absorption.

This is where structured solid targets come into play. Structured targets may provide better laser-target coupling [67,68], edge field amplification [69], laser guidance [70,71], and self-consistent ion injection into acceleration scheme [72]. For

---

[*] klezhnin@princeton.edu

instance, in [33], a solid target with holed conical opening and concave rear side with a proton layer doping was considered. The acceleration mechanism was attributed to a combination of TNSA and additional acceleration by the electric field of focused protons. Conical opening enhanced TNSA by a more effective hot electron generation on the rear side. A similar target, but with a plane rear side and comprised of high-Z ions was also discussed in [34]. High-Z ions and microchannel structure were implemented to improve hot electron generation and avoid laser filamentation, respectively. We note that using thin foil targets with holes for laser ion acceleration has been actively studied theoretically and experimentally in Refs. [73–75]. Microchannel target filled with relativistically transparent foam was considered in [76]. Laser pulse was tightly focused into the channel, propagated through relativistically transparent plasma while delivering significant energy to electrons from the channel filling and solid target walls, and exited from the rear side. The fastest ions were generated on the rear side of the target at the moment when defocusing laser pulse started to exit the channel. Channel target filled with relativistically transparent foam was also considered in [77–80] for efficient generation of $\gamma$ rays via synchrotron emission of fast electrons in quasistatic megatesla-scale magnetic field generated by laser-foam interaction. These targets are experimentally available and provide flexibility for particular experimental needs [60,68,81].

In this paper, we explore laser ion acceleration from structured solid targets filled with relativistically transparent plasma by means of particle-in-cell (PIC) simulations and theoretical estimates. We find optimal conditions for high-energy proton generation theoretically and verify them using comprehensive 2D PIC scans. The dominant acceleration mechanism is interpreted as a combination of TNSA and RPA across the broad set of laser and target parameters. We also conduct 3D PIC simulations and address such experimentally relevant questions as prepulse physics, oblique incidence, laser pointing stability, and the role of field ionization of the target. The role of the channel and solid target electrons is also discussed, as well as the role of radiation reaction (RR) for higher laser pulse powers. Finally, we discuss the scalability of the discussed acceleration scheme to the parameters of currently available channel targets [60,68,80].

This paper is structured as follows. Section II focuses on theoretical estimates for the maximum energy of protons from classical electrodynamics with and without the inclusion of radiation reaction force. Optimal target conditions for the given laser pulse parameters are also derived. Section III is devoted to the discussion of the simulation setup. In Sec. IV, we discuss the results of our 2D and 3D PIC scans and compare them with our theoretical interpretation. Other important aspects, such as prepulse effects, field ionization, oblique incidence, and pointing stability, are also addressed. Finally, we conclude with Sec. V by discussing our main results and comparing them with the literature.

## II. THEORY OF ION ACCELERATION FROM CHANNEL TARGETS

First, let us recall the concept of relativistic transparency, which is important for the considered ion acceleration scheme. As is well known, in a nonrelativistic case, the electromagnetic wave does not propagate into cold unmagnetized plasma if $\omega_{\rm pe} \geqslant \omega_0$. Here, $\omega_{\rm pe}^2 = 4\pi n_e e^2/m_e$ is the square of the plasma frequency for a nonrelativistic case. Thus, since in our case the channel density is $\sim 10^0 - 10^1 n_{\rm cr}$, where $n_{\rm cr} = m_e\omega_0^2/4\pi e^2$ is the critical density for the electromagnetic wave of frequency $\omega_0$, we should have expected from nonrelativistic considerations that the laser should reflect from the target. However, the relativistic motion of electrons relaxes the wave penetration condition due to an additional factor in the denominator of plasma frequency: $\omega_{\rm pe,rel}^2 = 4\pi n_e e^2/\langle\gamma_e\rangle m_e = \omega_{\rm pe}^2/\langle\gamma_e\rangle$, with $\langle\gamma_e\rangle$ being an average electron gamma factor, that effectively decreases the threshold for laser pulse propagation in classically overcritical plasma. Since electrons in the laser pulse gain average energy of $m_e c^2 a_0$, where $a_0 = eE_0/m_e\omega_0 c$ is the normalized amplitude of the laser pulse, we expect $\langle\gamma_e\rangle \approx a_0$, leading to $\omega_{\rm pe,rel} = \omega_{\rm pe}/\sqrt{a_0}$ (see Ref. [82]). For tightly focused petawatt-scale laser pulses, it will lead to the relativistic transparency of the channel for laser pulse, thus providing efficient conditions for laser-target coupling.

Following [53], let us derive the optimal condition for ion acceleration. First, the total energy of the laser pulse is

$$\mathcal{E}_{\rm las,0} = I_0 a_0^2 \pi w^2 \tau_{\rm las}, \tag{1}$$

where $I_0 = 1.384 \times 10^{18}\ {\rm W/cm^2}$ and $\tau_{\rm las}$ is the duration of the laser pulse, and $w$ is the waist of the laser pulse. This energy is fixed for a particular laser pulse. At the same time, the total energy of the electrons in the channel after the partial absorption of the pulse may be estimated by the formula

$$\mathcal{E}_{\rm ele} = m_e c^2 a_0 n_{\rm ch} \pi R_{\rm ch}^2 L_{\rm ch}, \tag{2}$$

where $n_{\rm ch}$, $R_{\rm ch}$, and $L_{\rm ch}$ are channel electron number density, radius, and length, respectively. By equating (1) and (2), we get an optimal condition for ion acceleration in the case of magnetically assisted TNSA (MVA) [53,54]. The leftover energy of the pulse after propagation through the channel (if any) will be responsible for the second stage of ion acceleration. For simplicity, we assume that the radiation pressure acceleration is responsible for the second stage of ion acceleration within the whole parameter range considered in the paper, although it should be noted that other acceleration mechanisms, such as RITA [47] and CSA [55], may contribute at particular parameter subspace. We discuss the role of these two mechanisms in Sec. V. To calculate the leftover laser energy, let us assume that the energy dissipation in the channel happens in such a way that only affects the field amplitude. The energy of the laser pulse after exiting the channel will look like the following:

$$\mathcal{E}_{\rm las,ch} = \mathcal{E}_{\rm las,0} - \mathcal{E}_{\rm ele} = I_0 a_{\rm ch}^2 \pi w^2 \tau_{\rm las}. \tag{3}$$

In the case of high laser intensities, we may also want to include energy losses due to radiation reaction in consideration. As is well known [83], in the near-critical density plasma for dimensionless field amplitudes

$$a_0 \geqslant \left(\frac{3\lambda m_e c^2}{4\pi e^2}\right)^{1/3}, \tag{4}$$

(for $\lambda = 1\ \mu$m wavelength laser the radiation intensity should be above $10^{23}\ {\rm W/cm^2}$) the radiation reaction force becomes important. The energy lost by electromagnetic pulse propagating in plasma may be estimated as follows. A single electron maximum radiation power may be calculated as $\mathcal{P}_{\rm RR} = eEc$. Total energy lost to radiation would be

$$\mathcal{E}_{\rm RR} = \mathcal{P}_{\rm RR} n_{\rm ch} \pi w^2 \tau_{\rm las} L_{\rm ch} = \mathcal{E}_{\rm ele}. \tag{5}$$

The remaining laser pulse energy that will accelerate ions via radiation pressure

$$\mathcal{E}_{\rm las,ch+RR} = \mathcal{E}_{\rm las,0} - \mathcal{E}_{\rm ele} - \mathcal{E}_{\rm RR} = I_0 a^2_{\rm ch+RR} \pi w^2 \tau_{\rm las}. \tag{6}$$

Now, let us optimize the maximum ion energy obtainable in the considered ion acceleration scheme. For simplicity, we ignore the RR losses for now. The maximum energy gained from TNSA-like acceleration may be estimated as (following [26])

$$\Delta\mathcal{E}_{\rm TNSA} \approx \alpha T_{\rm e,nth} = \alpha m_e c^2 \Big(\sqrt{1 + a_0^2} - 1\Big) \approx \alpha m_e c^2 a_0, \tag{7}$$

where $\alpha$ is a dimensionless constant larger than 1, which accounts for the finite size of the accelerating field, energy cutoff of nonthermal electron energies in the rear side of the channel, and possible superponderomotive electron temperatures (e.g., see [34]). This constant is to be determined by simulations. In the limit of the ultrarelativistic ion energy, the energy gained from RPA can be estimated as (e.g., see Ref. [12])

$$\Delta\mathcal{E}_{\rm RPA} \approx m_e c^2 a_0^2 \frac{n_{\rm cr} c \tau_{\rm las}}{n_0 l_0}, \tag{8}$$

where $n_0$ and $l_0$ are the density and the thickness of the foil target, and $n_{\rm cr} = m_e \omega_0^2 / 4\pi e^2$. In our case, there is no foil target, but the hole boring by the laser pulse creates a dense foil-like structure with the thickness $\sim\lambda$ at the end of the channel. Assuming that this structure is comprised of the channel electrons, we write a condition on $n_0$ and $l_0$: $n_0 l_0 \approx L_{\rm ch} n_{\rm ch}$. In order to estimate the energy gain by an ion from RPA in a nonoptimized target case, we multiply this expression by a function $\Xi = f(a_{\rm ch}, \frac{n_{\rm ch}}{n_{\rm cr}}, \frac{L_{\rm ch}}{\lambda})$ that will isolate an optimal regime of RPA ion acceleration, $a_0 \approx n_{\rm ch}/n_{\rm cr} L_{\rm ch}/\lambda$, and exponentially damp the acceleration away from "the resonance condition", i.e., it is equal to one for optimal RPA condition and quickly tends to zero outside of it. For comparison with PIC simulations, we took the particular shape of this function to be $\Xi = \exp{[-(\frac{a_{\rm ch}}{n_{\rm ch}/n_{\rm cr} L_{\rm ch}/\lambda} - 1)^2]}$. Finally, we multiply this expression by dimensionless constant $K$, which controls the efficiency of RPA acceleration (i.e., the reflectivity of the foil accelerated by RPA) and will be determined from simulations as well. The total energy gain by a single proton may be estimated as

$$\begin{aligned} \mathcal{E}_{\rm max} &= \Delta\mathcal{E}_{\rm TNSA} + \Delta\mathcal{E}_{\rm RPA} \approx \\ & m_e c^2 \bigg\{ \alpha a_0 + K a^2_{\rm ch} \frac{n_{\rm cr}}{n_{\rm ch}} \frac{c\tau_{\rm las}}{L_{\rm ch}} \Xi\Big(a_{\rm ch}, \frac{n_{\rm ch}}{n_{\rm cr}}, \frac{L_{\rm ch}}{\lambda}\Big)\bigg\}, \end{aligned} \tag{9}$$

where

$$a^2_{\rm ch} = a_0^2 - a_0 \frac{m_e c^3 n_{\rm cr}}{I_0} \frac{R^2_{\rm ch}}{w^2} \frac{n_{\rm ch}}{n_{\rm cr}} \frac{L_{\rm ch}}{c\tau_{\rm las}} \tag{10}$$

is the laser field dimensionless amplitude after the depleted laser pulse exits the channel (here we neglect RR energy losses). Maximizing $\mathcal{E}_{\rm max}$ will give an optimal condition for ion acceleration. Since the energy gain is dominated by the RPA mechanism, we may approximately claim that the optimal condition is

$$a_{\rm ch} \approx \frac{n_{\rm ch}}{n_{\rm cr}} \frac{L_{\rm ch}}{\lambda}. \tag{11}$$

Now, let us describe a simple model to explain the maximum ion energy scaling with time. As noted above, we assume that the ions are first accelerated by TNSA electric field, and further accelerated by RPA, and the total energy gain is $\mathcal{E}_{\rm max} = \Delta\mathcal{E}_{\rm TNSA} + \Delta\mathcal{E}_{\rm RPA}$. We assume TNSA acceleration to be instantaneous, and the evolution of ion energy under the radiation pressure is calculated as in Refs. [38,40]: We start with a 1D model and write down the equation of motion of plasma under the influence of radiation pressure,

$$\partial_\tau p = \mathcal{P} \frac{1 - \beta}{1 + \beta}, \tag{12}$$

$$\beta = \frac{p}{\sqrt{1 + p^2}}. \tag{13}$$

Here, $p$ is normalized to $m_i c$, $\tau \equiv t/T_0$ ($T_0 = \lambda/c$ is the laser period), and the radiation pressure is given by

$$\mathcal{P} = K \frac{m_e}{m_i} a_0^2 \frac{n_{\rm cr}}{n_e} \frac{\lambda}{l_0}. \tag{14}$$

$K$ here is a free dimensionless parameter [same as in Eq. (9)] that controls the laser-target interaction efficiency. Asymptotic solution for ultrarelativistic ions, $p \propto t^{1/3}$, is well known [38]. However, here we do not expect ions to gain ultrarelativistic energies, so we solve Eqs. (12) and (13) with $p(t = 0) = p_{\rm TNSA}/m_i c = \sqrt{2\mathcal{E}_{\rm TNSA}/m_i c^2}$, i.e., the initial ion momentum is gained from TNSA fields. We see that the channel parameters and laser amplitude appear in $\mathcal{P}$, and $p(0)$ also implicitly depends on channel parameters. We fit the resulting $p(t; \alpha, K, t_0)$ trajectories from simulations with free parameters $\alpha, K, t_0$. It turns out that the model describes $p(t)$ from simulations fairly well, with $\alpha \sim 3 - 5$, $K \sim 0.1 - 0.3$, $t_0 \approx t_{\rm exit}$, with $t_{\rm exit}$ being the time of laser pulse exiting the channel from the rear end.

## III. SIMULATION SETUP

To check the theoretical considerations from the previous section and consider a more realistic physical scenario, we perform 2D and 3D particle-in-cell (PIC) simulations using the code EPOCH [84,85]. Numerical setup and illustration of typical 2D/3D simulation results are shown in Fig. 1. All the parameters we scan on are summarized in Table I. For 2D runs, we consider Gaussian laser pulses with laser wavelength $\lambda = 1\ \mu$m, laser durations $\tau = 30$ and 150 fs, $w = 1.1 - 15\ \mu$m waist, and linear polarization ($B_z$ is out of simulation plane $x$-$y$) focused onto the channel entrance at $x = 10\ \mu$m. The laser pulse power spans from 0.3 to 30 PW, covering the range of dimensionless amplitudes, $a_0$, from 25 to 850 (peak intensities range from $10^{21}$ to $3 \times 10^{23}$ W/cm$^2$). The target locates between $x = 10\ \mu$m and $10\mu$m $+ \mathrm{L_{ch}}$, where $L_{\rm ch}$ is the channel length, which varies from 10 to 100 micron. Solid wall density equals to $100 - 300 n_{\rm cr}$. The channel has the radius $R_{\rm ch} = 1 - 10\mu$m, and is filled with uniform plasma with $n_{\rm ch} = 0 - 40 n_{\rm cr}$. The plasma is comprised of electrons and protons with zero initial temperature. The simulation box

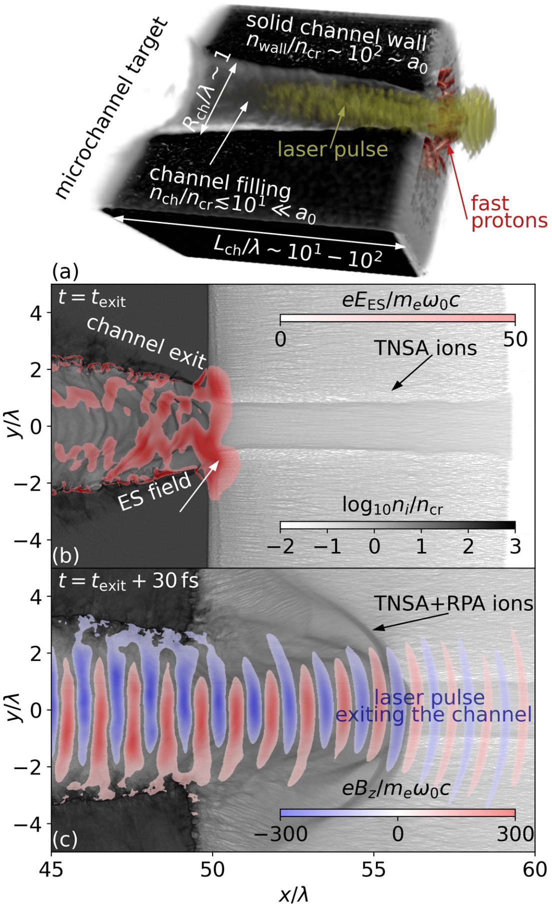

FIG. 1. (a) Result of 3D PIC simulation with $P = 10$ PW, $L_{\text{ch}} = 40\ \mu\text{m}$, and $n_{\text{ch}} = 10 n_{\text{cr}}$. Primary free parameters of the problem are indicated. [(b),(c)] Illustration of acceleration scheme from 2D PIC run for $P = 10$ PW and $L_{\text{ch}} = 40\ \mu\text{m}$: Electrostatic field, evolution of ion density, and laser field at time of laser pulse exiting the channel ($t = t_{\text{exit}}$) and 30 femtoseconds later are shown.

TABLE I. 2D PIC scan parameters.

| | Range |
|---|---|
| Laser parameters: | |
| Peak power $P$, PW | $0.3 - 30$ |
| Pulse duration $\tau_{\text{las}}$, fs | 30, 150 |
| Waist $w$, $\mu$m | $1.1 - 15$ |
| Laser wavelength $\lambda$, $\mu$m | 1 |
| Contrast $I_{\text{prepulse}}/I_{\max}$ | 0.0, $10^{-6} - 10^{-3}$ |
| Prepulse duration, ps | 1 |
| Target parameters: | |
| Channel radius $R_{\text{ch}}/\lambda$ | $1 - 10$ |
| Channel length $L_{\text{ch}}/\lambda$ | $10 - 100$ |
| Filling density $n_{\text{ch}}/n_{\text{cr}}$ | 0–40 |
| Solid wall density $n_{\text{wall}}/n_{\text{cr}}$ | 100, 300 |
| Target front cut angle, ° | 0, 15, 45 |
| General parameters: | |
| Simulation box size $\lambda \times \lambda$ | $200 \times 30$ |
| Grid resolution $1/\lambda$ | 60 |
| Particle resolution, ppc | 20, 40, 80 |
| Total simulation time, ps | 1.5–2.5 |
| Radiation reaction term | on & off |
| Field ionization | on & off |

dimension is $(160\lambda + L_{\text{ch}}) \times 30\lambda$ with the numerical resolution of 60 grid nodes per $\lambda$. The resolution ensures that typical plasma wavelength, $\lambda_{\text{pe}} = 2\pi c/\omega_{\text{pe}}$, is resolved with 6 grid nodes. The boundary conditions are outflow for both axes. The number of particles per cell is 20–80 per species. We conduct runs with radiation reaction (RR) terms turned on and off to see its influence on ion acceleration.

To address the case with realistic target material, e.g., solid Kapton substrate and CH foam as the channel filling [80], we considered CH targets with $L_{\text{ch}} = 20 - 50\lambda$, $R_{\text{ch}} = 1.8\ \lambda$, $w = 2.2\lambda$, $n_{\text{e,wall}} = 300 n_{\text{cr}}$, $n_{\text{e,ch}} = 10 - 30 n_{\text{cr}}$, and fully ionized C and H atoms.

We also considered oblique incidence by adding a cut to the front side of the target. Oblique incidence ensures the absence of the backreflection of the laser pulse, which is safer for possible application on laser facilities [60,68]. We consider a cut with 10° and 45° angles on the front of the target while keeping all other simulation parameters the same as described above.

For 3D simulations, following [76], we consider 1 PW and 10 PW, 150 fs Gaussian linear polarized pulses focused onto the channel target entrance onto the 2.2-micron spot. The considered target parameters are similar to ones in 2D simulations, with $L_{\text{ch}} = 20 - 30\ \mu\text{m}$, $n_{\text{wall}}/n_{\text{cr}} = 100$, $R_{\text{ch}} = 1.8\ \mu\text{m}$, and $n_{\text{ch}}/n_{\text{cr}} = 10$, comprised of protons are electrons.

Finally, for auxiliary radiation hydrodynamics simulations using FLASH code, we inherited the LaserSlab simulation setup [86,87], which considers the interaction of laser beam with the typical nanosecond laser pedestal parameters with the solid aluminum target. In our case, we conducted a set of analogous runs with only modifications being the modified density profile—we introduced a channel of $R_{\text{ch}} = 3\ \mu\text{m}$ at the axis of $R - z$ simulation plane in cylindrical coordinates—and polystyrene (CH) target corresponding to $n_{\text{e,wall}} = 300 n_{\text{cr}}$ and $n_{\text{e,ch}} = 20 n_{\text{cr}}$, while also expanding the simulation box to 120 $\mu$m along $z$ axis, resulting in $40\lambda \times 120\lambda$ dimensions in $R - z$ space, with the channel located between $z = 40\lambda$ and $80\lambda$. The laser pulse has the wavelength of 1 $\mu$m, Gaussian transverse shape with the e-folding length of 3 $\mu$m, and focused onto the center of the channel entrance with normal incidence. The temporal profile of the laser pulse has a linear ramp of 0.1 ns from 0 to peak power and duration of 0.9 ns with the total simulation time being 1 ns. We varied the peak laser pedestal power, covering the range from $10^5$ to $10^9$ W. This corresponds to laser contrasts from $10^{-11}$ to $10^{-7}$ for 10 PW driver pulse. The resulting density snapshots from these simulations were mirrored around the $z$ axis, zoomed in to $-20\lambda$ to $20\lambda$ in the transverse direction, and inserted into 2D PIC code EPOCH to analyze a possible detrimental role of the prepulse on laser ion acceleration.

## IV. SIMULATION RESULTS

First, let us discuss the typical 2D PIC simulation result for $P = 1$ PW, $n_{\text{ch}}/n_{\text{cr}} = 10$, $L_{\text{ch}} = 30\ \mu\text{m}$, $w = 1.1\ \mu\text{m}$, and $R_{\text{ch}} = 1\ \mu\text{m}$. Figure 2 illustrates the physics of the two-stage acceleration process. It combines 1D profiles of longitudinal electric field $E_x/E_0$ (averaged over $1\mu\text{m}$ in the transverse direction, i.e. over the central half-channel; electric field is measured in $E_0 = m_e\omega_0 c/e$), 1D envelope of the laser pulse

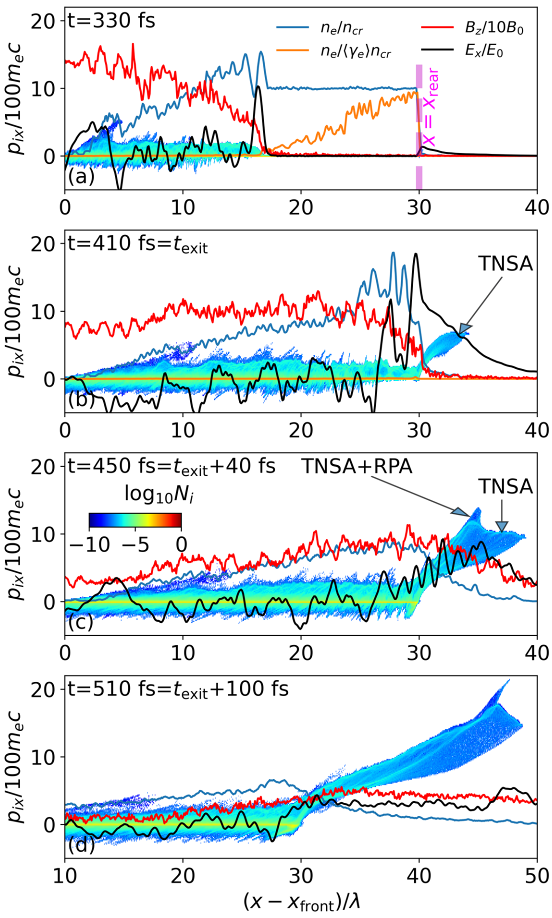

FIG. 2. Evolution of ion phase space in $x - p_{\rm ix}$ coordinates (colormap), along with 1D profiles of electron density (blue), electron density normalized to average electron gamma (orange), laser envelope (red), and longitudinal electric field (black). (a) t = 330 fs, laser pulse propagates in the channel, a significant laser-electron coupling is seen—electrons are not evacuated from the channel, the channel is relativistically transparent—sustaining a significant electron density well above $n_{\rm cr}$; (b) t = 410 fs, laser pulse reaches the rear end of the target, accelerating electric field builds up on the rear part of the target, TNSA accelerated ions are seen; (c) t = 450 fs, laser pulse leaves the channel and provides an additional acceleration of ions; rapid acceleration of ion filament from the rear side of the channel is seen (annotated as TNSA+RPA); (d) t = 510 fs, the most rapid phase of ion acceleration is over [see Fig. 4(a), green line], but ions continue to gradually gain more energy via RPA.

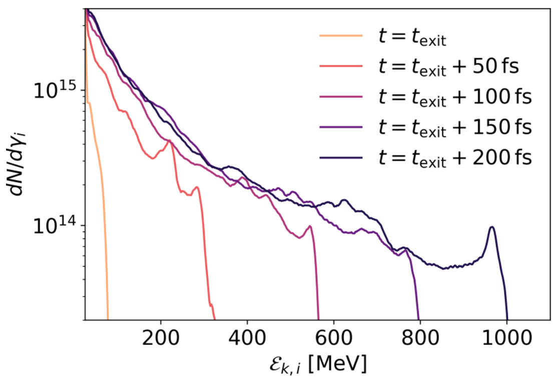

FIG. 3. Proton spectrum evolution for the simulation with $P = 1$ PW, $L_{\rm ch} = 40\ \mu$m, $n_{\rm ch} = 10n_{\rm cr}$. The development of the high-energy spectrum and the quasimonoenergetic peak is seen after the laser pulse starts to exit the channel.

at $y = 0$, $B_z/10E_0$, 1D profile of electron density $n_e/n_{\rm cr}$ (averaged over 1 $\mu$m in the transverse direction as well) and $x - p_{\rm ix}$ phase space plot for t = 330, 410, 450, 510 fs. The laser pulse is focused onto the front side of the channel, and since $n_e/\langle\gamma_e\rangle \ll n_{\rm cr}$ [orange lines in Figs. 2(a) and 2(b)], the pulse will propagate into the channel without significant back-reflection. Also, since the channel density is relativistically transparent, it is not completely wiped out by ponderomotive forces and always stays well above nonrelativistic critical density $n_{\rm cr}$, thus providing better laser-electron coupling [blue lines in Figs. 2(a)–2(d)]. Once the pulse reaches the rear part of the target at t = 410 fs, we observe a build-up of a strong longitudinal electric field (predominantly, electrostatic) up to $E_x/E_0 \approx 20$. At this time, ion phase space exhibits an onset of TNSA-like acceleration at the rear end of the target [Fig. 2(b), $x \approx 45\ \mu$m; also Fig. 1(b) for a 2D density map of ions accelerated solely by TNSA]. However, the fastest ions in the simulation are generated promptly at the time of laser pulse exiting the rear side of the channel [see Fig. 2(c), spike at $x \approx 45\ \mu$m]. These ions are accelerated by the TNSA field first, and then further accelerated by RPA [Figs. 1(c) and 2(d)].

Figure 3 represents the time evolution of proton spectrum for target with $L_{\rm ch} = 40\ \mu$m, $n_{\rm ch} = 10n_{\rm cr}$ and laser pulse peak power of $P =$ 1PW. At the final time, $t = t_{\rm exit} + 200$ fs, there is a relatively flat spectrum in the high-energy range, with a peak around the maximum ion energy. Time evolution of the spectrum reveals that the peak in the ion spectrum is developed at the time of the laser pulse exiting from the rear side of the channel. Further acceleration is achieved by the direct acceleration of ions by laser pulse via RPA, as suggested by Fig. 2(d) and Figs. 4(a) and 4(b).

Figures 4(a) and 4(b) shows maximum ion energy as a function of time for 1 PW and 10 PW laser pulses for the selected channel lengths from 10 to 100 $\mu$m. By fitting the curves from Figs. 4(a) and 4(b), we see that they are closely followed by the theoretical model described in Sec. II, and tend to have the same late-time scaling as RPA (measured scaling is $p_i \propto t^{0.37}$, which is close to RPA's $p_i \propto t^{1/3}$). Figures 4(c) and 4(d) demonstrate how maximum ion energy depends on $L_{\rm ch}$. It is seen that there is an optimal channel length, in accordance with Eq. (11). Our theoretical model fairly predicts an optimal channel length [shaded regions in Figs. 4(c) and 4(d)].

From Eq. (11) it is also seen that there is an optimal channel density. Figure 5 shows how maximum ion energy depends on channel filling density $n_{\rm ch}$ for a fixed set of other parameters. While also predicting the existence of an optimal channel density, the agreement is worse than for a channel length $L_{\rm ch}$. This may be explained by an effectively different channel density at the rear end of the channel, which is a combination of initial channel filling that stayed inside the channel and channel solid wall parts that were extracted by the intense laser pulse. Analyzing an average electron density at the rear end of the channel (i.e., inside the channel within

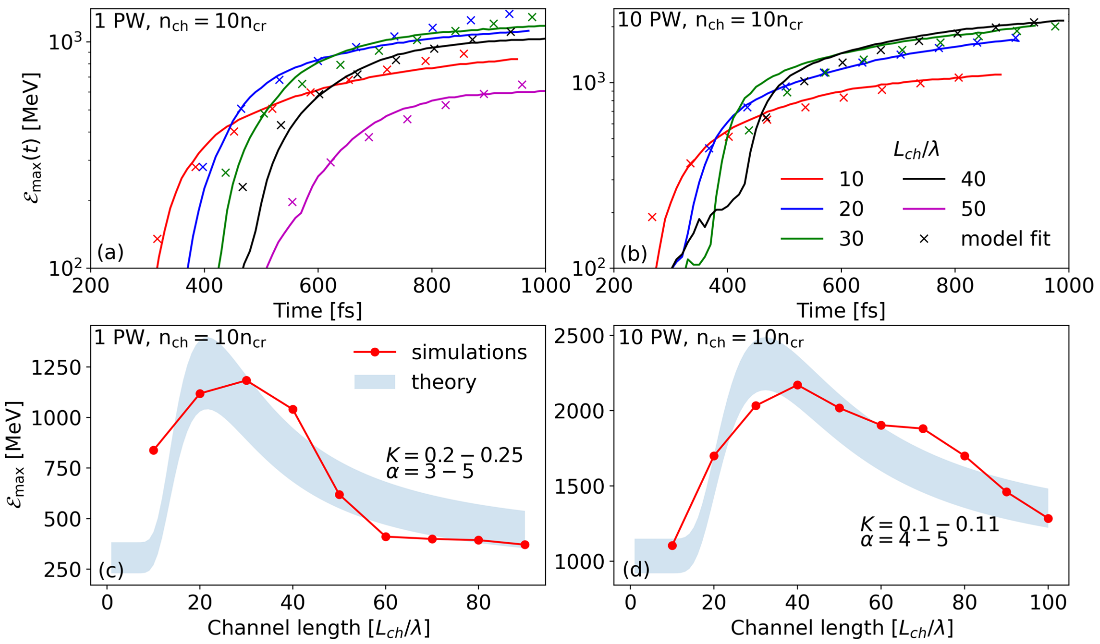

FIG. 4. Time evolution of maximum ion energy [(a), (b)] and channel length scan vs maximum ion energy [(c), (d)] for 1 PW peak laser pulse power (left) and 10 PW peak laser pulse power (right). Crosses and shaded region denote theoretical predictions for maximum ion energy temporal evolution and maximum ion energy as the function of channel length, respectively.

2λ from the channel rear end), we found that at the time of the laser pulse exiting the channel, the electron density there turns out to be almost identical for initial channel density fillings in the range $n_{ch}/n_{cr} = 0 - 10$, see Fig. 6. Simulations with tagged channel filling and wall electrons [Fig. 6(b)] explicitly demonstrate that the contribution of channel filling is negligible in comparison to wall electrons that end up at the rear part of the channel. Additionally, the variance of the maximum ion energy with respect to channel filling density is less than 25% for $n_{ch} \leqslant 30n_{cr}$. To conclude, the channel filling density plays a relatively minor role in ion acceleration, which implies relaxed requirements on the laser contrast for the described laser ion acceleration scheme.

To elaborate on the role of the laser contrast for the considered target, we perform an additional set of 2D PIC simulations, where a Gaussian prepulse of picosecond duration is added before the primary pulse, with the laser contrast, $I_{prepulse}/I_{max}$, varied from $10^{-6}$ to $10^{-3}$. While the duration of the prepulse may reach up to nanosecond duration [88], which is beyond reach for the conventional PIC codes, significant damage to the target may be done by spontaneous prepulses of shorter duration, such as a considered picosecond prepulse [88]. We examine the cases of $P = 1\&10$ PW, $n_{ch}/n_{cr} = 0, 1, 10, 20$. The variations in maximum ion energy with contrast are no more than 25%, with higher contrast runs

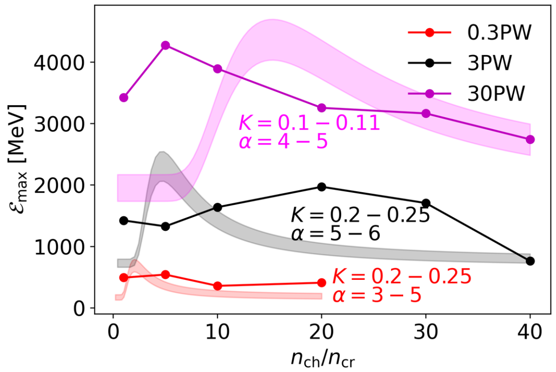

FIG. 5. Dependence of maximum ion energy on channel filling density for pulses from 0.3 to 30 PW. Shaded regions illustrate theoretical predictions for maximum ion energies as the function of channel filling density.

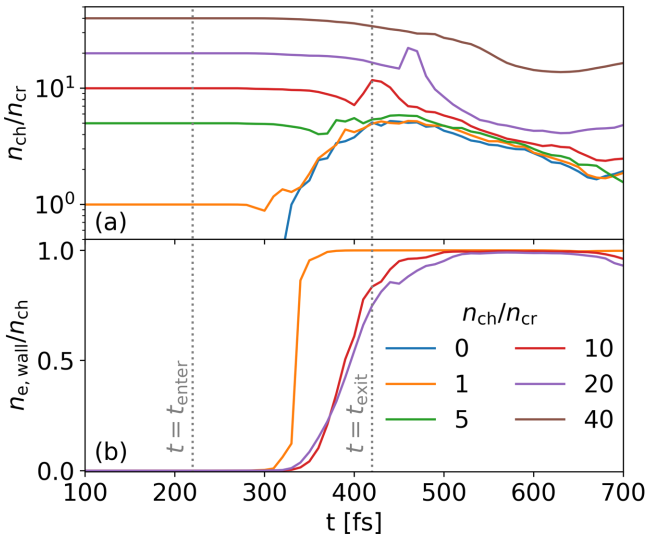

FIG. 6. (a) Evolution of the average channel density at the exit of the channel for $P = 1$ PW and (b) evolution of the fraction of the wall electrons in the average density at the exit of the channel for $P = 10$ PW. The build-up of the universal density value for all simulations with $n_{ch}/n_{cr} \leqslant 10$ and dominance of the wall electrons contributing to ion acceleration are seen.

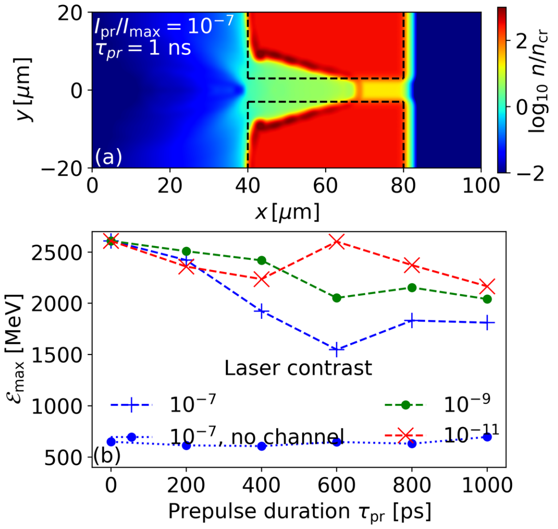

FIG. 7. (a) Electron density snapshot from FLASH simulation of nanosecond pedestal-target interaction for the case of laser contrast of $10^{-7}$. Dashed-black lines sketch the initial location of the channel structure. (b) Maximum ion energy dependence on pedestal duration for different laser contrasts ($10^{-11}$, $10^{-9}$, $10^{-7}$) and no channel case for laser contrast $10^{-7}$.

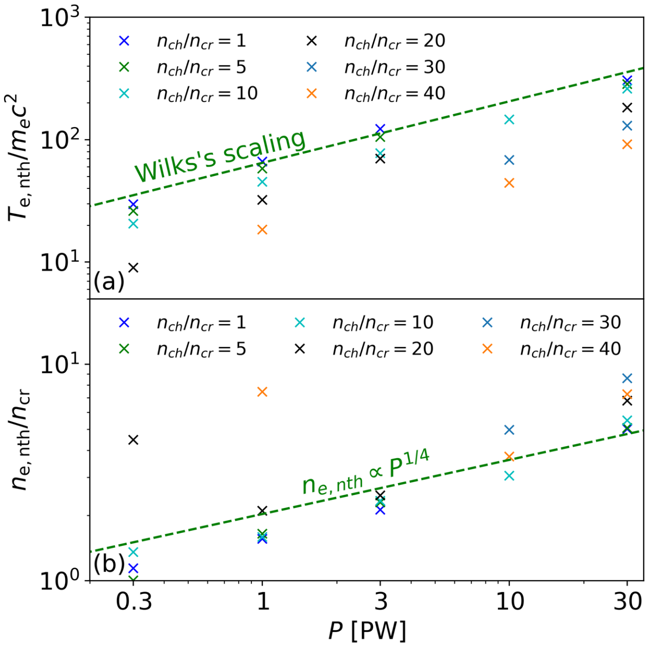

FIG. 8. Scalings of (a) electron nonthermal temperature, $T_{\mathrm{e,nth}}$ and (b) density $n_{\mathrm{e,nth}}$ with laser power. Wilks' scaling and waveguide model [green-dashed lines in (a) and (b), respectively] fairly explain the simulation results.

typically overperforming the corresponding runs with lower contrast. The overall acceleration mechanism seems to be unaffected by the considered prepulse.

To verify the robustness of the acceleration scheme against realistic laser contrast effects, we conducted a set of radiation hydrodynamics simulations using FLASH code [86] for the parameters described in Sec. III. Obtaining a set of density snapshots for 0.2–1 ns into the laser pedestal-CH target interaction, we initialized 2D PIC runs with these density snapshots and compared the resulting maximum proton energies at the end of 2D PIC runs. Figure 7(a) shows the electron density snapshot from the FLASH run for the case of $10^{-7}$ laser contrast and 1 ns into the simulation. We may see that while the target density departed from the initial channel structure location shown in dashed black lines, the overall structure of the target remains intact. Figure 7(b) reveals the effect of the laser pedestal on the maximum ion energies obtained in these simulations. We find that the presence of the pedestal with $\leqslant$400 ps duration and contrast no worse than $10^{-7}$ keeps the peak ion energy within the 75% of the ideal case of no prepulse. Thus, we may conclude that the realistic laser contrast of moderate level does not reduce the efficiency of the acceleration mechanism. A set of FLASH+PIC runs with the uniform CH target was also considered, delivering significantly diminished peak ion energies [circle-dotted-blue line in Fig. 7(b)]. A more detailed analysis of radiation hydrodynamics + PIC pipeline simulations is required for better matching experimental conditions of a particular laser facility, including realistic 3D geometry, target material, and oblique incidence. These questions are beyond the scope of this paper and will be addressed separately.

For a better understanding of the TNSA stage of ion acceleration, it is of interest to calculate the average density and temperature of hot electrons to the right from the rear end of the channel. Figure 8 demonstrates the scaling of nonthermal electron population parameters with laser pulse power. Figure 8(a) shows such dependence for the nonthermal temperature ($T_{\mathrm{e,nth}} \equiv \langle \mathcal{E}_e \rangle$) and compares it to the established scalings [34]. Figure 8(b) reveals calculations of average nonthermal electron density, $n_{\mathrm{e,nth}}$, and compares it against the waveguide model [34]. Overall, the nonthermal temperature measured in all simulations is in fair agreement with Wilks' scaling [26], $T_{\mathrm{e,nth}} \propto \sqrt{1 + a_0^2} - 1 \approx a_0$. $n_{\mathrm{e,nth}}$ scaling is fairly captured by the waveguide model, although the best fit suggests a stronger dependence of nonthermal electron density on laser power. It may be explained by different optimal target parameters $L_{\mathrm{ch}}$ and $n_{\mathrm{ch}}$ for the considered range of laser pulse powers $P = 0.3 - 30$ PW. Backtracking all electrons that end up with kinetic energies larger than 500 MeV for $P = 10$ PW, $L_{\mathrm{ch}} = 40\ \mu$m, $n_{\mathrm{ch}} = 20 n_{\mathrm{cr}}$ run, we found that they mainly originate from the front side of the channel walls [see Fig. 9(a)], specifically, from two lobes centered around $x = 15\lambda$, $y = \pm 2 - 3\lambda$, which is within the limits predicted by waveguide theory ($d_e = c/\omega_{\mathrm{pe}} \approx \lambda\sqrt{a_0 n_{\mathrm{cr}}/n_{\mathrm{wall}}}/2\pi \sim \lambda$). Simulations with smaller $P$ and/or $n_{\mathrm{ch}}$ lead to a similar conclusion. Figure 9(b) exemplifies a few trajectories of the fastest electrons in the simulation. They also originate from solid target walls and enter the oscillation cycle in the involved configuration of laser and background fields [89–91], effectively gaining energy at the channel exit. Finally, we calculated the relative role of channel filling and wall electrons in the TNSA accelerating field by comparing $\sqrt{n_{\mathrm{e,nth}} T_{\mathrm{e,nth}}}$ for each electron population. The fraction of channel filling contribution to the electrostatic field was found to be no more than 30%, thus further suggesting a secondary role of channel filling.

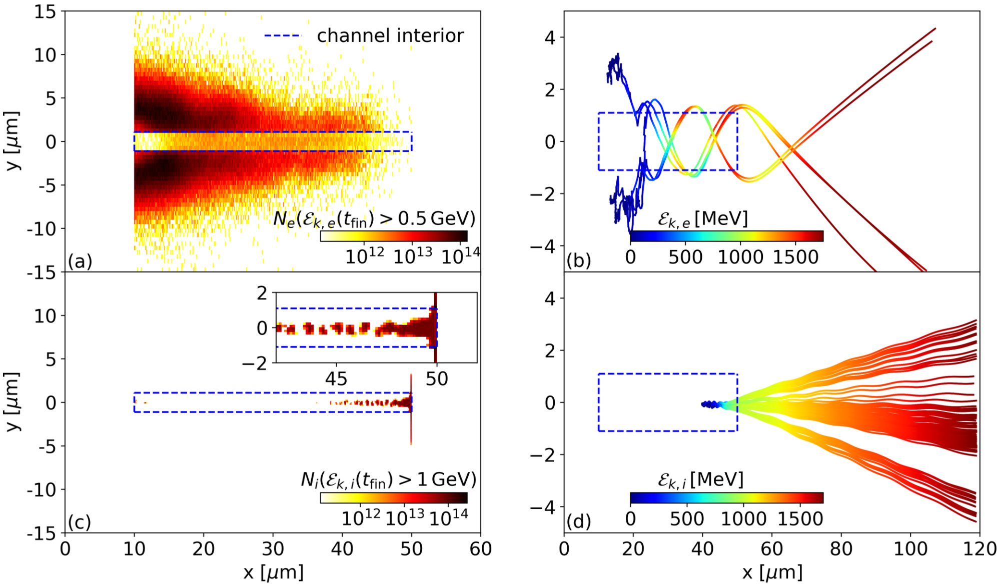

FIG. 9. Histograms of original location of (a) fastest electrons (ones that end up with kinetic energy >500 MeV) and (c) fastest ions (>1 GeV); fast electron (b) and ion (d) tracks for the simulation with $P = 10$ PW, $L_{\rm ch} = 40\ \mu$m, and $n_{\rm ch}/n_{\rm cr} = 20$. Blue-dashed lines denote the initial location of the channel interior.

It is also worth discussing where the fast ions originated. In order to do so, we conducted (1) a simulation with $P = 10$ PW, $n_{\rm ch}/n_{\rm cr} = 20$, $L_{\rm ch} = 40\,\mu$m with a full tracking of ion trajectories and (2) a set of simulations with $P = 10$ PW, $L_{\rm ch} = 40\,\mu$m, varying $n_{\rm ch}/n_{\rm cr}$ from 0 to 40 and tagging channel filling and wall ions. The first run suggested that the fastest ions (ones that ended up with kinetic energy exceeding 1 GeV) are predominantly from the rear end of the channel filling [see Fig. 9(c)], while a small yet non-negligible fraction originated from the channel walls within a few microns from the channel rear end. Analogous runs with the smaller filling density of $n_{\rm ch}/n_{\rm cr} = 1$ or smaller laser pulse power $P = 1$ PW are in qualitative agreement with this finding. The channel filling density scan with tagged particles revealed that the high-energy end of the ion spectrum (ions with 100 MeV or more) is comprised of both filling and wall ions for all runs, with wall ions dominating in $n_{\rm ch}/n_{\rm cr} \leqslant 10$ range and filling ions being abundant for $n_{\rm ch}/n_{\rm cr} \geqslant 20$, including the case of optimal channel filling density. Figure 9(d) shows a few tracks of fast ions that ended up with $\mathcal{E}_{k,i} \approx 1.5$ GeV accelerated from the rear end of the target, again verifying the two-stage nature of the ion acceleration scheme: It acts both at the rear end of the target and further away from the sheath field.

As one may see from Eq. (9), the contribution from channel radius and beam waist to the maximum attainable ion energy is connected to the energy transfer efficiency of the laser pulse with the constant beam waist to the channel filling electrons under the assumption that the channel does not significantly evolve. In reality, however, these assumptions do not hold, as we see from our runs with varying initial beam waists and channel radii. When channel radius $R_{\rm ch}$ is significantly larger than beam waist at focus $w$, laser pulses experience transverse filamentation and hosing instabilities [92], leading to the reduced ion acceleration efficiency. At the same time, for $w > R_{\rm ch}$, the laser energy may be partially scattered from the channel entrance, decreasing the acceleration efficiency. Figure 10(a) presents our scan on laser beam waist for $P = 10$ PW laser pulse and $n_{\rm ch} = 20n_{\rm cr}$ target with $R_{\rm ch} = 2, 6, 10\lambda$. The relativistic transparency condition that may be written as $w < w_t \equiv 0.85\sqrt{10^5 P[\mathrm{PW}]/(n_{\rm ch}/n_{\rm cr})}$ is found to be satisfied for the considered focal spot values, triggering relativistic transparency of the channel in practically all laser powers and channel filling densities from Table I. A sweet spot in Fig. 10(a) is found around $w_{\rm opt} \approx 2-3\mu$m for all channel radii considered. This is close to the radius of self-channeling laser pulse in uniform plasma given by $R_{\rm sc}/\lambda = 3.44(n_{\rm cr}/n_{\rm ch})^{1/3}(P[\mathrm{PW}])^{1/6} \approx 1.86$ [53]. Focusing on the spot close to the smallest between self-channeling radius $R_{\rm sc}$ and channel wall radius $R_{\rm ch}$ helps to transmit high laser amplitude through the whole channel length, leading to higher proton energies. Comparing with the theoretical model fit given by Eq. (9), we see that the peak ion energy drops as the laser amplitude is inversely proportional to the laser spot, $a_0 \propto w^{-1}$. The maximum energy dropoff with the laser waist tends to be linear rather than quadratic, as one may expect from RPA scaling [38]. This may be attributed to the elevated hot electron population generated by wider laser spot size, improving the TNSA regime. Overall, laser focusing to a few $\lambda$ spot, which is within reach for modern laser facilities [93], delivers optimal peak proton energies.

Transverse laser pointing stability influences ion acceleration in the following manner. When the laser beam completely misses the channel cross section, i.e., when the absolute value of the laser axis pointing shift $\delta y$ is equal to or larger than $R_{\rm ch} + w/2$, the TNSA mechanism is realized with an increased hot electron population due to presence of the channel. When the laser beam spot is within the channel cross-section, i.e., when $|\delta y| \leqslant R_{\rm ch} - w/2$, there should be no changes in maximum ion energy according to the proposed theoretical model. For the pointing shifts in between these two values, the maximum ion energy is obtained from the two-stage mechanism with the effectively reduced laser pulse power, $P_{\rm ch} \approx P(0.5 + (R_{\rm ch} - \delta y)/w)^{N-1}$, where $N$ is

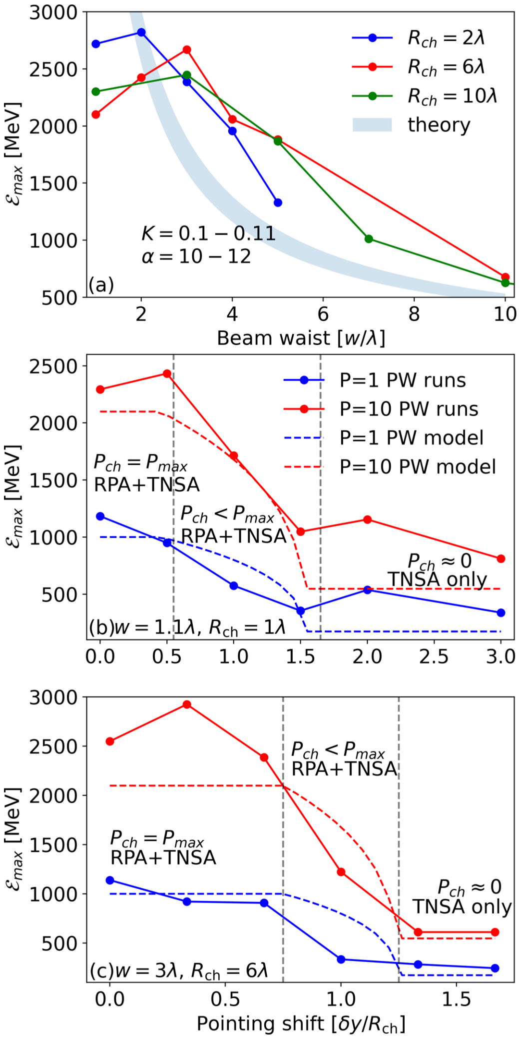

FIG. 10. (a) Dependence of maximum ion energy on beam waist for different channel radii $R_{\rm ch} = 2 - 10\mu$m for $P = 10$ PW, $L_{\rm ch} = 40$ $\mu$m, $n_{\rm ch} = 20n_{\rm cr}$ simulations. The shaded region represents theoretical prediction. Maximum ion energy dependence on laser axis shift $\delta y$ for $P = 1$ PW (blue) and 10 PW (red) for (b) $R_{\rm ch} = 1\lambda$, $w = 1.1\lambda$ and (c)$R_{\rm ch} = 6\lambda$, $w = 3\lambda$. Red- and blue-dashed lines represent the predictions of the theoretical model, grey-dashed lines separate out different acceleration regimes.

the dimensionality of the problem. The maximum ion energy is calculated from our theoretical model for $P_{\rm ch} > 0$ and from classical scaling $\mathcal{E}_{\rm max} = 173$ MeV$\sqrt{\rm P[PW]}$ for $P_{\rm ch} = 0$ [20]. Figures 10(b) and 10(c) compare our simulation results for pointing stability scan for $R_{\rm ch} = 1$ $\mu$m, $w = 1.1$ $\mu$m and $R_{\rm ch} = 6$ $\mu$m and $w = 3$ $\mu$m with our interpretation. The agreement is satisfactory, with the largest discrepancy appearing in the case of TNSA-only accelerated ions. The final requirement on maximum pointing shift is $|\delta y| \leqslant \delta y_{\rm max} = R_{\rm ch} - w/2$, which may be satisfied on the modern laser facilities for the majority of shots [94–96].

To understand the possible range of applicability of the considered acceleration scheme, it is of interest to check such a target on the maximum energy scaling with laser pulse power. Figure 11 summarizes the whole set of our simulations.

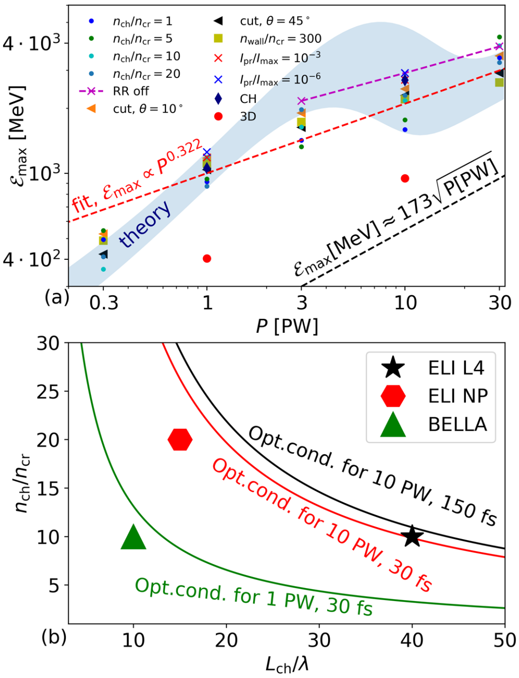

FIG. 11. (a) Maximum energy scaling with power. Different markers represent different channel densities; the crossed-dashed-magenta line corresponds to the simulations with RR off. We also plot typical energy scalings—classical theoretical scaling [20] (black-dashed line). The fit of maximum ion energies observed in our runs (red-dashed line) is also shown. (b) Optimal target conditions for ELI L4, ELI-NP, and BELLA lasers from 2D PIC simulations (markers) and theory predictions [Eq. (11), solid lines].

It turns out that the scaling derived in Sec. II (shaded region) is in approximate agreement with simulations. Maximum proton energies are well above the usual theoretical scaling for maximum proton energy (black-dashed line) [20]. The universal fitting formula for maximum ion energy scaling may be written as

$$\mathcal{E}_{\rm max} = \left(\frac{\rm P}{1\,\rm PW}\right)^{0.322} \rm GeV. \qquad (15)$$

Runs with RR off demonstrate a factor of a few advantage in terms of maximum ion energy in contrast to RR on simulations (cross-dashed magenta line in Fig. 11), which is expected as the additional laser energy losses given by Eq. (5) diminish both TNSA and RPA efficiency.

We also considered a cut on the front side of the target, having a wedge with $\theta = 10^\circ$ and $45^\circ$ angle on its front. It is evident that such a cut does not suppress ion acceleration (orange and black triangles in Fig. 11), and may be helpful for the experimental realization of the proposed acceleration scheme by avoiding hazardous laser backreflection [60,68]. A slight decrease in maximum ion energy for the cut of $45^\circ$ may be interpreted on a basis of Fig. 9(a), where the cut of a target front may effectively decrease the efficiency of hot electron generation by suppressing $n_{\rm e,nth}$.

The additional runs with the increased wall density ($n_{\rm wall}/n_{\rm cr} = 300$) do not differ much from our main set of simulations with $n_{\rm wall}/n_{\rm cr} = 100$, since the dependence of channel wall skin depth on the solid target density is pretty weak, $d_e \propto n_{\mathrm{wall}}^{-1/2}$. As a result, fast electron generation is not affected, leading to similar values of $\mathcal{E}_{\max}$ (squares in Fig. 11). Likewise, considering a realistic CH target with $n_{\mathrm{wall}}/n_{\mathrm{cr}} = 300$ and $n_{\mathrm{ch}}/n_{\mathrm{cr}} = 20$ [80], we observe the same level of maximum proton energies [diamond markers in Fig. 11(a)] and ion acceleration mechanism.

Field ionization was also included in a separate series of 2D PIC runs. Both picosecond prepulse and driver pulse are capable of fully ionizing the part of the channel responsible for ion acceleration, and the maximum ion energies are not affected for all considered laser pulse powers. The presence of picosecond prepulses did not change the maximum attainable ion energies, as discussed earlier in the paper.

Finally, we conducted a series of 3D runs for $P = 1\&10$ PW laser pulses, which showed a factor of $\sim 2-3$ maximum proton energy dropoff in comparison to our 2D runs. Possible reasons for the diminished maximum proton energy could be weaker hot electron retention [97,98] and stronger constraints on the transparency of the accelerated foil [99]. Still, the main features of the acceleration mechanism, namely, rapid ion acceleration from the channel rear end at the time of laser pulse exiting the channel and presence of quasimonoenergetic structure in the ion energy spectrum were verified, in agreement with [76]. The dimensionality is also known to affect the group and phase velocities of the laser pulse, which may affect electron acceleration [100] and the RPA stage of ion acceleration [13], thus contributing to the maximum proton energy dropoff. Our analysis of the TNSA stage of ion acceleration suggests that it is not significantly affected by the group velocity changes due to the channel filling density variations, as seen from Fig. 8. The RPA stage of the acceleration scheme happens after the laser pulse exits from the channel rear, thus, the maximum ion energy is not limited by the group velocity of the laser.

## V. SUMMARY AND DISCUSSION

In this paper, we considered laser ion acceleration from the micron-scale channels filled with relativistically transparent plasma. We obtained an optimal set of parameters for such acceleration and proposed a model to predict the ion energy gain with time. These considerations were checked against 2D PIC simulations and are in fair agreement with them across the wide parameter range covered by simulations. A few experimentally relevant physical effects were also addressed. The main results may be listed as follows:

(i) The acceleration is interpreted as a combination of TNSA and RPA, illustrated by Figs. 1 and 2.

(ii) Quasimonoenergetic features in the wide high-energy proton spectra are observed, as shown in Fig. 3. The time of quasimonoenergetic structure development coincides with the time of the laser pulse exiting the channel.

(iii) A simple theoretical model is developed on a basis of [12,26,53]. Optimal interaction conditions are given by Eq. (11), in approximate agreement with 2D PIC scans on channel length $L_{\mathrm{ch}}$ and channel filling density $n_{\mathrm{ch}}$, depicted by Figs. 4 and 5.

(iv) The role of laser contrast is investigated, both indirectly, via the analysis of the role of channel filling electrons, and directly, with picosecond prepulse PIC simulations and auxiliary radiation hydrodynamics simulations of nanosecond pedestal coupled with PIC (Fig. 7). Figures 5 and 6 illustrate the relaxed conditions on the channel filling density, while Figs. 8 and 9 discuss the role of channel filling on electron heating.

(v) Channel radius requirements are shown to be a nonrestrictive factor in the discussed acceleration scheme, see Fig. 10(a), which is beneficial for the currently available channel targets [80].

(vi) The acceleration mechanism is shown to be robust against moderate perturbations in laser pointing, see Figs. 10(b) and (c), in fair agreement with the model.

(vii) Oblique incidence (i.e., a cut at the front surface of the target) and field ionization were shown to be insignificant limitations for maximum ion energies.

(viii) In our 2D PIC scan, we observed GeV-scale protons accelerated by PW-scale laser pulses with approximate energy scaling $\mathcal{E}_{\max} \propto P^{0.322}$, seen in Fig. 11.

(ix) Finally, three-dimensional simulations verified the primary features of the acceleration scheme, though the maximum ion energies are less than in analogous 2D cases.

One may argue that the suboptimal power scaling questions the applicability of structured targets. While power scaling was found to be quite shallow (Eq. 15, in contrast to theoretical scalings, $\mathcal{E}_{\max,\mathrm{TNSA}} \propto P^{1/2}$ for TNSA [26,32] and $\mathcal{E}_{\max,\mathrm{RPA}} \propto P$ for RPA [38]), for $P \leqslant 1$PW the acceleration mechanism is competitive with other mechanisms in terms of maximum ion energies (factor of a few larger than for analogous laser parameters in the TNSA regime [32] and around the same values as from RPA [39], MVA [53], and laser ion shotgun acceleration [76]). While the theoretically predicted performance of RPA is well above our numerical results [40] for $P > 1$ PW, the proposed scheme provides robustness to the acceleration mechanism with respect to laser envelope modulations, laser contrast, and oblique incidence effects that would be detrimental for the performance of pure RPA acceleration with ultrathin targets [58]. Moreover, an additional analysis suggested that the considered acceleration mechanism possesses a high laser-to-proton energy conversion efficiency of no less than 15%, promising a high volumetric charge of fast ion beam [76]. This feature of the discussed acceleration scheme may be beneficial for the fast ignition concept in inertial confinement fusion [6,101].

In comparison to uniform near-critical density targets (or, for the channels with channel radius significantly exceeding beam waist, $R_{\mathrm{ch}} \gg w$), channel targets provide better pulse guiding and larger counts of fast protons [76]. Auxiliary simulations with a uniform near-critical target with $n_e = 1 - 40 n_{\mathrm{cr}}$ show that the fast ion population is an order of magnitude smaller than for the channel target, along with a notable laser pulse hosing, detrimental for the resulting angular distribution of the ion source.

Quasistatic magnetic fields produced by micron-scale channel targets are remarkable—they exist on a picosecond scale, and demonstrate maximum values $B_{\max}^{\mathrm{QS}} \approx 110\ \mathrm{kT}(P[\mathrm{PW}])^{0.2}$ even after the pulse exits the channel, closely reaching the megatesla-scale magnetic fields recently predicted in laser-driven microtube implosions [102]. These fields are known to significantly modify the electron motion inside the channel, allowing for a steady energy gain [61], and may provide a platform for experiments with $\gamma$-ray generation and pair production [77,78,80]. The obtained $B_{\rm max}^{\rm QS}$ values are smaller than $B_{\rm max}^{\rm QS} \approx 550\ {\rm kT}(P[{\rm PW}])^{0.5}$ suggested by Eqs. (2) and (3) in [76] due to the difference in the magnetic field measurement methodology.

It is worth noting that magnetic vortex acceleration (MVA) mechanism may also contribute to the ion acceleration at the rear side of the target. Indeed, as we observe a strong quasi-static magnetic field forming inside the channel, we may expect the dipole structure to expand out of the channel exit, thus maintaining the charge separation and corresponding sheath field. However, since the considered channel length is smaller than the optimal pulse dissipation length for MVA obtained by equating Eqs. (1) and (2) [53], and the solid wall density preventing the magnetic vortex expansion, we believe that the MVA is suppressed in our acceleration scheme.

Another acceleration mechanism that may naturally appear at the rear side of the target is CSA [55]. In such an acceleration regime, it is assumed that the collisionless shock structure is formed by the laser pulse acting as a piston via the ponderomotive forces, and the shock structure reflects ions by the cross-shock electrostatic potential, resulting in $u_{p0} + 2v_{\rm sh}$ jump in ion velocity in the nonrelativistic case ($u_{\rm p0}$ is the initial proton velocity, $v_{\rm sh}$ is the shock speed in laboratory frame). We estimated the typical ion energy gain one may expect from CSA in case of $P = 10$ PW, $L = 40\lambda$, $n_{\rm ch} = 20n_{\rm cr}$. The shock speed from our simulation is estimated by calculating $\langle v_{\rm i}\rangle$ and taking the maximum value across the channel; it results in $v_{\rm sh} \approx 0.4c$. Assuming the reflected protons start from rest in the laboratory frame, we get the reflected proton velocity in the laboratory frame, $v_{\rm p} = 2v_{\rm sh}/(1 + v_{\rm sh}^2/c^2) \approx 0.69c$, which corresponds to $\Delta\mathcal{E}_{\rm CSA} \approx 350$ MeV. This constitutes about 18% of the maximum proton energy obtained in the respective simulation, as seen from Fig. 11(a). Moreover, estimating the cross-shock potential, we find that it is close to the energy of the incoming ion in the shock frame, $e\Delta\Phi = e\int_{\rm shock} E_x dx \approx \mathcal{E}_{\rm sh} = m_i c^2(\gamma_{\rm sh} - 1)$, which implies that the ion reflection from the shock is limited. Thus, we conclude that CSA provides only a minor contribution to the fast ion energy budget in the optimal parameter regime, and thereby it is not included in our interpretation of the simulation results. One may also imagine that the RITA regime may manifest itself within the subspace of the parameter range we considered in our simulations. We note, though, that the RITA typically appears in the case of ultrathin ($\sim 10^1 - 10^2$ nm; [47,48]) or relatively thin ($\leqslant 5\lambda$; [103]) targets. Moreover, synchronization between the laser pulse and the onset of the relativistic transparency is required for the appearance of RITA, which is often lost within our numerical scan—a foil exiting from the rear side of the target quickly becomes opaque and its density stays well above $n_{\rm cr}$, thus missing the most efficient stage of RITA [104]. Another possible signature of RITA, the three population structure of the ion $x - p_x$ phase plot [103], does not seem to appear in our simulations, which typically have two fast ion populations, as seen in Fig. 2, which better matches the TNSA and TNSA+RPA acceleration schemes (see Fig. 2(c) in [103]). Thus, we conclude that while RITA may be the most efficient ion acceleration mechanism in some of our runs, for simplicity, we decided to apply the TNSA+RPA interpretation uniformly across the whole set of laser and target parameters.

When choosing the parameters for the simulations, we aimed at those that will soon be available at ELI-Beamlines L4 ATON laser [17]. Based on our analytical model, we may envision an efficient application of the discussed acceleration scheme with laser parameters of ELI-NP [105], Apollon [18], J-KAREN-P [106], and BELLA [96] as well. Figure 11(b) shows optimal structured target conditions for these lasers obtained through auxiliary 2D PIC scans and theoretically predicted optimal regime given by Eq. (11). The agreement between them is fair, though the maximum proton energy for 1 PW, 30 fs laser pulse is significantly suppressed, being no more than 600 MeV.

Finally, let us discuss how the considered target compares to the microstructure targets produced today. In [80], a very similar type of target was considered, with the primary differences being channel dimensions and material. Our results suggest that the maximum ion energy will be suppressed for the channels of $L_{\rm ch} \sim 100\ \mu$m manufactured for the gamma ray generation [80], giving a preference for channels of approximately half of that size, as seen in Figs. 4(c) and 4(d). Scans on channel radius [Fig. 10(a)] and pointing stability [Figs. 10(b) and 10(c)] predict a promising scaling to realistic parameters $R_{\rm ch} = 6\ \mu$m and $\sqrt{\delta y^2} = 5\ \mu$m [80] (microchannel array target and OMEGA EP laser parameters), sustaining the acceleration efficiency. ELI L3 [94,95] and BELLA [96] lasers reported $<2.5\ \mu$rad and $<1.2\ \mu$rad pointing stability, respectively, corresponding to $<2\mu$m beam target displacement, which also satisfies the $|\delta y| \leqslant \delta y_{\rm max}$ criterion. Our simulations with increased solid wall density ($n_{\rm e,wall} = 300n_{\rm cr}$) and high-Z runs for polystyrene target (radiation hydrodynamics + 2D PIC simulations) and CH target [2D PIC simulations; diamonds in Fig. 11(a)] suggest that the considered laser ion acceleration scheme will be applicable for the Kapton substrate-CH foam filling targets as well, in agreement with [76].

The results obtained in the paper show that the considered laser ion acceleration scheme is robust against moderate variations in laser and target parameters, thus making it a viable candidate for experimental implementation.

## ACKNOWLEDGMENTS

This work was supported by NNSA Grants No. DE-NA0003871, No. DE-SC0021248, and by the Project High Field Initiative (CZ.02.1.01/0.0/0.0/15 003/0000449) from European Regional Development Fund. The EPOCH code was developed as part of the UK EPSRC funded Projects EP/G054940/1. The software used in this work was developed in part by the DOE NNSA- and DOE Office of Science-supported Flash Center for Computational Science at the University of Chicago and the University of Rochester. The simulations presented in this article were performed on computational resources managed and supported by Princeton Research Computing at Princeton University. K.V.L. is thankful to Alexey Arefiev for fruitful discussions.

[1] C. N. Danson, C. Haefner, J. Bromage, Th. Butcher, J.-C. F. Chanteloup, E. A. Chowdhury, A. Galvanauskas, L. A. Gizzi, J. Hein, D. I. Hillier *et al.*, Petawatt and exawatt class lasers worldwide, High Power Laser Sci. Eng. **7**, e54 (2019).

[2] H. Daido, M. Nishiuchi, and A. S. Pirozhkov, Review of laser-driven ion sources and their applications, Rep. Prog. Phys. **75**, 056401 (2012).

[3] A. J. Mackinnon, P. K. Patel, R. P. Town, M. J. Edwards, T. Phillips, S. C. Lerner, D. W. Price, D. Hicks, M. H. Key, S. Hatchett *et al.*, Proton radiography as an electromagnetic field and density perturbation diagnostic, Rev. Sci. Instrum. **75**, 3531 (2004).

[4] S. V. Bulanov and V. S. Khoroshkov, Feasibility of using laser ion accelerators in proton therapy, Plasma Phys. Rep. **28**, 453 (2002).

[5] S. V. Bulanov, T. Zh. Esirkepov, V. S. Khoroshkov, A. V. Kuznetsov, F. Pegoraro, Oncological hadrontherapy with laser ion accelerators, Phys. Lett. A **299**, 240 (2002).

[6] M. Roth, T. E. Cowan, M. H. Key, S. P. Hatchett, C. Brown, W. Fountain, J. Johnson, D. M. Pennington, R. A. Snavely, S. C. Wilks *et al.*, Fast Ignition by Intense Laser-Accelerated Proton Beams, Phys. Rev. Lett. **86**, 436 (2001).

[7] M. Nishiuchi, H. Sakaki, T. Zh. Esirkepov, K. Nishio, T. A. Pikuz, A. Ya. Faenov, I. Yu. Skobelev, R. Orlandi, H. Sako, A. S. Pirozhkov *et al.*, Acceleration of highly charged GeV Fe ions from a low-Z substrate by intense femtosecond laser, Phys. Plasmas **22**, 033107 (2015).

[8] A. J. Gonsalves, K. Nakamura, J. Daniels, C. Benedetti, C. Pieronek, T. C. H. de Raadt, S. Steinke, J. H. Bin, S. S. Bulanov, J. van Tilborg *et al.*, Petawatt Laser Guiding and Electron Beam Acceleration to 8 GeV in a Laser-Heated Capillary Discharge Waveguide, Phys. Rev. Lett. **122**, 084801 (2019).

[9] T. Tajima and J. M. Dawson, Laser Electron Accelerator, Phys. Rev. Lett. **43**, 267 (1979).

[10] T. Esirkepov, M. Yamagiwa, and T. Tajima, Laser Ion-Acceleration Scaling Laws Seen in Multiparametric Particle-in-Cell Simulations, Phys. Rev. Lett. **96**, 105001 (2006).

[11] A. Macchi, M. Borghesi, and M. Passoni, Ion acceleration by superintense laser-plasma interaction, Rev. Mod. Phys. **85**, 751 (2013).

[12] S. V. Bulanov, J. J. Wilkens, T. Zh. Esirkepov, G. Korn, G. Kraft, S. D. Kraft, M. Molls, and V. S. Khoroshkov, Laser ion acceleration for hadron therapy, Phys. Usp. **57**, 1149 (2014).

[13] S. S. Bulanov, E. Esarey, C. B. Schroeder, S. V. Bulanov, T. Zh. Esirkepov, M. Kando, F. Pegoraro, and W. P. Leemans, Radiation pressure acceleration: The factors limiting maximum attainable ion energy, Phys. Plasmas **23**, 056703 (2016).

[14] A. Higginson, R. J. Gray, M. King, R. J. Dance, S. D. R. Williamson, N. M. H. Butler, R. Wilson, R. Capdessus, C. Armstrong, J. S. Green *et al.*, Near-100 MeV protons via a laser-driven transparency-enhanced hybrid acceleration scheme, Nat. Commun. **9**, 724 (2018).

[15] P. L. Poole, L. Obst, G. E. Cochran, J. Metzkes, H.-P. Schlenvoigt, I. Prencipe, T. Kluge, T. Cowan, U. Schramm, D. W. Schumacher, and K. Zeil, Laser-driven ion acceleration via target normal sheath acceleration in the relativistic transparency regime, New J. Phys. **20**, 013019 (2018).

[16] K. A. Tanaka, K. M. Spohr, D. L. Balabanski, S. Balascuta, L. Capponi, M. O. Cernaianu, M. Cuciuc, A. Cucoanes, I. Dancus, A. Dhal *et al.*, Current status and highlights of the ELI-NP research program, Matter Radiat. Extremes **5**, 024402 (2020).

[17] B. Rus, P. Bakule, D. Kramer, J. Naylon, J. Thoma, M. Fibrich, J. T. Green, J. C. Lagron, R. Antipenkov, J. Bartoníček *et al.*, ELI-beamlines: Progress in development of next generation short-pulse laser systems, Proc. SPIE **10241**, 102410J-1 (2017).

[18] D. N. Papadopoulos, J. P. Zou, C. Le Blanc, G. Chériaux, P. Georges, F. Druon, G. Mennerat, P. Ramirez, L. Martin, A. Fréneaux *et al.*, The Apollon 10 PW laser: Experimental and theoretical investigation of the temporal characteristics, High Power Laser Sci. Eng. **4**, e34 (2016).

[19] M. Kaluza, J. Schreiber, M. I. K. Santala, G. D. Tsakiris, K. Eidmann, J. Meyer-ter-Vehn, and K. J. Witte, Influence of the Laser Prepulse on Proton Acceleration in Thin-Foil Experiments, Phys. Rev. Lett. **93**, 045003 (2004).

[20] T. Zh. Esirkepov, J. K. Koga, A. Sunahara, T. Morita, M. Nishikino, K. Kageyama, H. Nagatomo, K. Nishihara, A. Sagisaka, H. Kotaki *et al.*, Prepulse and amplified spontaneous emission effects on the interaction of a petawatt class laser with thin solid targets, Nucl. Instrum. Methods Phys. Res., Sect. A **745**, 150 (2014).

[21] P. Hadjisolomou, I. P. Tsygvintsev, P. Sasorov, V. Gasilov, G. Korn, and S. V. Bulanov, Preplasma effects on laser ion generation from thin foil targets, Phys. Plasmas **27**, 013107 (2020).

[22] M. Nishiuchi, N. P. Dover, M. Hata, H. Sakaki, K. Kondo, H. F. Lowe, T. Miyahara, H. Kiriyama, J. K. Koga, N. Iwata, M. A. Alkhimova, A. S. Pirozhkov, Y. Faenov, T. A. Pikuz, A. Sagisaka, Y. Watanabe, M. Kando, K. Kondo, E. J. Ditter, O. C. Ettlinger *et al.*, Dynamics of laser-driven heavy-ion acceleration clarified by ion charge states, Phys. Rev. Res. **2**, 033081 (2020).

[23] J. Ferri, E. Siminos, L. Gremillet, and T. Fülöp, Effects of oblique incidence and colliding pulses on laser-driven proton acceleration from relativistically transparent ultrathin targets, J. Plasma Phys. **86**, 905860505 (2020).

[24] L. Ding, S. Li, Z. Lu, Y. Wang, C. Zhu, Y. Chen, P. Du, H. Zhang, C. Cui, L. Zhou *et al.*, Analysis of the beam-pointing stability in the high power laser system, Optik **127**, 6056 (2016).

[25] M. Tamburini, F. Pegoraro, A. Di Piazza, C. H. Keitel, and A. Macchi, Radiation reaction effects on radiation pressure acceleration, New J. Phys. **12**, 123005 (2010).

[26] S. C. Wilks, A. B. Langdon, T. E. Cowan, M. Roth, M. Singh, S. Hatchett, M. H. Key, D. Pennington, A. MacKinnon, and R. A. Snavely, Energetic proton generation in ultra-intense laser–solid interactions, Phys. Plasmas **8**, 542 (2001).

[27] M. Passoni, L. Bertagna, and A. Zani, Target normal sheath acceleration: Theory, comparison with experiments and future perspectives, New J. Phys. **12**, 045012 (2010).

[28] G. A. Becker, S. Tietze, S. Keppler, J. Reislöhner, J. H. Bin, L. Bock, F.-E. Brack, J. Hein, M. Hellwing, P. Hilz *et al.*, Ring-like spatial distribution of laser accelerated protons in the ultra-highcontrast TNSA-regime, Plasma Phys. Control. Fusion **60**, 055010 (2018).

[29] F. Bisesto, M. Galletti, M. P. Anania, G. Costa, M. Ferrario, R. Pompili, A. Zigler, F. Consoli, M. Cipriani, M. Salvadori, and C. Verona, Simultaneous observation of ultrafast electron and

proton beams in TNSA, High Power Laser Sci. Eng. **8**, e23 (2020).

[30] R. A. Simpson, D. A. Mariscal, J. Kim, G. G. Scott, G. J. Williams, E. Grace, C. McGuffey, S. Wilks, A. Kemp, N. Lemos, B. Z. Djordjevic *et al.*, Demonstration of TNSA proton radiography on the national ignition facility advanced radiographic capability (NIF-ARC) laser, Plasma Phys. Control. Fusion **63**, 124006 (2021).

[31] J. Park, J. Kim, G. Cochran, D. Mariscal, R. A. Simpson, A. Zylstra, and T. Ma, Experimental verification of TNSA protons and deuterons in the multi-picosecond moderate intensity regime, Phys. Plasmas **29**, 063106 (2022).

[32] S. Keppler, N. Elkina, G. A. Becker, J. Hein, M. Hornung, M. Mäusezahl, C. Rödel, I. Tamer, M. Zepf, and M. C. Kaluza, Intensity scaling limitations of laser-driven proton acceleration in the TNSA-regime, Phys. Rev. Res. **4**, 013065 (2022)

[33] J.-L. Liu, Z. M. Sheng, J. Zheng, W. M. Wang, M. Y. Yu, C. S. Liu, W. B. Mori, and J. Zhang, Two-stage acceleration of protons from relativistic laser-solid interaction, Phys. Rev. ST Accel. Beams **15**, 101301 (2012).

[34] D. B. Zou, A. Pukhov, L. Q. Yi, H. B. Zhuo, T. P. Yu, Y. Yin, F. Q. Shao, Laser-driven ion acceleration from plasma microchannel targets, Sci. Rep. **7**, 42666 (2017).

[35] A. Yogo, S. V. Bulanov, M. Mori, K. Ogura, T. Zh. Esirkepov, A. S. Pirozhkov, M. Kanasaki, H. Sakaki, Y. Fukuda, P. R. Bolton, H. Nishimura, and K. Kondo, Ion acceleration via 'nonlinear vacuum heating' by the laser pulse obliquely incident on a thin foil target, Plasma Phys. Control. Fusion **58**, 025003 (2016).

[36] A. Yogo, K. Mima, N. Iwata, S. Tosaki, A. Morace, Y. Arikawa, S. Fujioka, T. Johzaki, Y. Sentoku, H. Nishimura *et al.*, Boosting laser-ion acceleration with multi-picosecond pulses, Sci. Rep. **7**, 42451 (2017).

[37] D. B. Zou, D. Y. Yu, X. R. Jiang, M. Y. Yu, Z. Y. Chen, Z. G. Deng, T. P. Yu, Y. Yin, F. Q. Shao, H. B. Zhuo, C. T. Zhou, and S. C. Ruan, Enhancement of target normal sheath acceleration in laser multi-channel target interaction, Phys. Plasmas **26**, 123105 (2019).

[38] T. Esirkepov, M. Borghesi, S. V. Bulanov, G. Mourou, and T. Tajima, Highly Efficient Relativistic-Ion Generation in the Laser-Piston Regime, Phys. Rev. Lett. **92**, 175003 (2004).

[39] A. P. L. Robinson, M. Zepf, S. Kar, R. G. Evans, and C. Bellei, Radiation pressure acceleration of thin foils with circularly polarized laser pulses, New J. Phys. **10**, 013021 (2008).

[40] S. V. Bulanov, E. Yu. Echkina, T. Zh. Esirkepov, I. N. Inovenkov, M. Kando, F. Pegoraro, and G. Korn, Unlimited Ion Acceleration by Radiation Pressure, Phys. Rev. Lett. **104**, 135003 (2010).

[41] S. Kar, M. Borghesi, S. V. Bulanov, M. H. Key, T. V. Liseykina, A. Macchi, A. J. Mackinnon, P. K. Patel, L. Romagnani, A. Schiavi, and O. Willi, Plasma Jets Driven by Ultraintense-Laser Interaction with Thin Foils, Phys. Rev. Lett. **100**, 225004 (2008).

[42] S. Kar, K. F. Kakolee, B. Qiao, A. Macchi, M. Cerchez, D. Doria, M. Geissler, P. McKenna, D. Neely, J. Osterholz, R. Prasad, K. Quinn, B. Ramakrishna, G. Sarri, O. Willi, X. Y. Yuan, M. Zepf, and M. Borghesi, Ion Acceleration in Multispecies Targets Driven by Intense Laser Radiation Pressure, Phys. Rev. Lett. **109**, 185006 (2012).

[43] A. Henig, S. Steinke, M. Schnürer, T. Sokollik, R. Hörlein, D. Kiefer, D. Jung, J. Schreiber, B. M. Hegelich, X. Q. Yan, J. Meyer-ter-Vehn, T. Tajima, P.V. Nickles, W. Sandner, and D. Habs, Radiation-Pressure Acceleration of Ion Beams Driven by Circularly Polarized Laser Pulses, Phys. Rev. Lett. **103**, 245003 (2009).

[44] C. Scullion, D. Doria, L. Romagnani, A. Sgattoni, K. Naughton, D. R. Symes, P. McKenna, A. Macchi, M. Zepf, S. Kar, and M. Borghesi, Polarization Dependence of Bulk Ion Acceleration from Ultrathin Foils Irradiated by High-Intensity Ultrashort Laser Pulses, Phys. Rev. Lett. **119**, 054801 (2017).

[45] W. J. Ma, I. J. Kim, J. Q. Yu, I. W. Choi, P. K. Singh, H. W. Lee, J. H. Sung, S. K. Lee, C. Lin, Q. Liao *et al.*, Laser Acceleration of Highly Energetic Carbon Ions Using a Double-Layer Target Composed of Slightly Underdense Plasma and Ultrathin Foil, Phys. Rev. Lett. **122**, 014803 (2019).

[46] A. McIlvenny, D. Doria, L. Romagnani, H. Ahmed, N. Booth, E. J. Ditter, O. C. Ettlinger, G. S. Hicks, P. Martin, G. G. Scott *et al.*, Selective Ion Acceleration by Intense Radiation Pressure, Phys. Rev. Lett. **127**, 194801 (2021)

[47] L. Yin, B. J. Albright, B. M. Hegelich, and J. C. Fernandez, GeV laser ion acceleration from ultrathin targets: The laser break-out afterburner, Laser Part. Beams **24**, 291 (2006).

[48] D. Jung, B. J. Albright, L. Yin, D. C. Gautier, B. Dromey, R. Shah, S. Palaniyappan, S. Letzring, H.-C. Wu, T. Shimada *et al.*, Scaling of ion energies in the relativistic-induced transparency regime, Laser Part. Beams **33**, 695 (2015).

[49] J. C. Fernandez, D. C. Gautier, C. Huang, S. Palaniyappan, B. J. Albright, W. Bang, G. Dyer, A. Favalli, J. F. Hunter, J. Mendez *et al.*, Laser-plasmas in the relativistic transparency regime: Science and applications, Phys. Plasmas **24**, 056702 (2017).

[50] E. Fourkal, I. Velchev, and C.-M. Ma, Coulomb explosion effect and the maximum energy of protons accelerated by high-power lasers, Phys. Rev. E **71**, 036412 (2005).

[51] A. V. Kuznetsov, T. Zh. Esirkepov, F. F. Kamenets, and S. V. Bulanov, Efficiency of ion acceleration by a relativistically strong laser pulse in an underdense plasma, Plasma Phys. Rep. **27**, 211 (2001).

[52] Y. Fukuda, A. Ya. Faenov, M. Tampo, T. A. Pikuz, T. Nakamura, M. Kando, Y. Hayashi, A. Yogo, H. Sakaki, T. Kameshima *et al.*, Energy Increase in Multi-MeV Ion Acceleration in the Interaction of a Short Pulse Laser with a Cluster-Gas Target, Phys. Rev. Lett. **103**, 165002 (2009).

[53] S. S. Bulanov, V. Yu. Bychenkov, V. Chvykov, G. Kalinchenko, D. W. Litzenberg, T. Matsuoka, A. G. R. Thomas, L. Willingale, V. Yanovsky, K. Krushelnick, and A. Maksimchuk, Generation of GeV protons from 1 PW laser interaction with near critical density targets, Phys. Plasmas **17**, 043105 (2010).

[54] J. Park, S. S. Bulanov, J. Bin, Q. Ji, S. Steinke, J.-L. Vay, C. G. R. Geddes, C. B. Schroeder, W. P. Leemans, T. Schenkel, and E. Esarey, Ion acceleration in laser generated megatesla magnetic vortex, Phys. Plasmas **26**, 103108 (2019).

[55] F. Fiuza, A. Stockem, E. Boella, R. A. Fonseca, and L. O. Silva, Laser-Driven Shock Acceleration of Monoenergetic Ion Beams, Phys. Rev. Lett. **109**, 215001 (2012).

[56] S. S. Bulanov, A. Brantov, V. Yu. Bychenkov, V. Chvykov, G. Kalinchenko, T. Matsuoka, P. Rousseau, S. Reed, V. Yanovsky,

D. W. Litzenberg, K. Krushelnick, and A. Maksimchuk, Accelerating monoenergetic protons from ultrathin foils by flat-top laser pulses in the directed-Coulomb-explosion regime, Phys. Rev. E **78**, 026412 (2008).

[57] B. Qiao, M. Zepf, M. Borghesi, B. Dromey, M. Geissler, A. Karmakar, and P. Gibbon, Radiation-Pressure Acceleration of Ion Beams from Nanofoil Targets: The Leaky Light-Sail Regime, Phys. Rev. Lett. **105**, 155002 (2010).

[58] B. Qiao, M. Zepf, M. Borghesi, B. Dromey, M. Geissler, A. Karmakar, and P. Gibbon, Dominance of Radiation Pressure in Ion Acceleration with Linearly Polarized Pulses at Intensities of $10^{21}$ W cm$^{-}$2, Phys. Rev. Lett. **108**, 115002 (2012).

[59] J. Goodman, M. King, R. Wilson, R. J. Gray, and P. McKenna, Optimisation of multi-petawatt laser-driven proton acceleration in the relativistic transparency regime, New J. Phys. **24**, 053016 (2022).

[60] J. Snyder, L. L. Ji, K. M. George, C. Willis, G. E. Cochran, R. L. Daskalova, A. Handler, T. Rubin, P. L. Poole, D. Nasir *et al.*, Relativistic laser driven electron accelerator using micro-channel plasma targets, Phys. Plasmas **26**, 033110 (2019).

[61] T. Wang, Z. Gong, A. Arefiev, Electron confinement by laser-driven azimuthal magnetic fields during direct laser acceleration, Phys. Plasmas **27**, 053109 (2020).

[62] A. Rousse, P. Audebert, J. P. Geindre, F. Falliès, J. C. Gauthier, A. Mysyrowicz, G. Grillon, and A. Antonetti, Efficient K$\alpha$ x-ray source from femtosecond laser-produced plasmas, Phys. Rev. E **50**, 2200 (1994).

[63] I. A. Andriyash, R. Lehe, A. Lifschitz, C. Thaury, J.-M. Rax, K. Krushelnick, and V. Malka, An ultracompact x-ray source based on a laser-plasma undulator, Nat. Commun. **5**, 4736 (2014).

[64] T. Nakamura, J. K. Koga, T. Zh. Esirkepov, M. Kando, G. Korn, and S. V. Bulanov, High-Power $\gamma$-Ray Flash Generation in Ultraintense Laser-Plasma Interactions, Phys. Rev. Lett. **108**, 195001 (2012).

[65] C. P. Ridgers, C. S. Brady, R. Duclous, J. G. Kirk, K. Bennett, T. D. Arber, A. P. L. Robinson, and A. R. Bell, Dense Electron-Positron Plasmas and Ultraintense $\gamma$ Rays from Laser-Irradiated Solids, Phys. Rev. Lett. **108**, 165006 (2012).

[66] T. Kluge, W. Enghardt, S. D. Kraft, U. Schramm, K. Zeil, T. E. Cowan, and M. Bussmann, Enhanced laser ion acceleration from mass-limited foils, Phys. Plasmas **17**, 123103 (2010).

[67] D. Margarone, O. Klimo, I. J. Kim, J. Prokupek, J. Limpouch, T. M. Jeong, T. Mocek, J. Psikal, H. T. Kim, J. Proska *et al.*, Laser-Driven Proton Acceleration Enhancement by Nanostructured Foils, Phys. Rev. Lett. **109**, 234801 (2012).

[68] M. Bailly-Grandvaux, D. Kawahito, C. McGuffey, J. Strehlow, B. Edghill, M. S. Wei, N. Alexander, A. Haid, C. Brabetz, V. Bagnoud *et al.*, Ion acceleration from microstructured targets irradiated by high-intensity picosecond laser pulses, Phys. Rev. E **102**, 021201(R) (2020).

[69] G. A. Askar'yan and S. V. Bulanov, Resonant and edge amplification of the electric field in the plasma resonance layer and acceleration of particles on plasma inhomogeneities, JETP Lett. **9**, 1243 (1983).

[70] H. Y. Wang, X. Q. Yan, M. Zepf, Collimated proton acceleration in light sail regime with a tailored pinhole target, Phys. Plasmas **21**, 063113 (2014).

[71] S. S. Bulanov, E. Esarey, C. B. Schroeder, S. V. Bulanov, T. Zh. Esirkepov, M. Kando, F. Pegoraro, and W. P. Leemans, Enhancement of Maximum Attainable Ion Energy in the Radiation Pressure Acceleration Regime Using a Guiding Structure, Phys. Rev. Lett. **114**, 105003 (2015).

[72] M. Murakami, Y. Hishikawa, S. Miyajima, Y. Okazaki, K. L. Sutherland, M. Abe, S. V. Bulanov, H. Daido, T. Zh. Esirkepov, J. Koga, M. Yamagiwa, and T. Tajima, Radiotherapy using a laser proton accelerator, in *Laser Driven Relativistic Plasmas Applied for Science, Industry, and Medicine: The 1st International Symposium*, edited by S. V. Bulanov and H. Daido, AIP Conf. Proc. No. 1024 (AIP, New York, 2008), p. 275.

[73] J. Psikal, J. Grym, L. Stolcova, and J. Proska, Hollow target for efficient generation of fast ions by ultrashort laser pulses, Phys. Plasmas **23**, 123121 (2016).

[74] P. Hadjisolomou, S. V. Bulanov, G. Korn, Towards laser ion acceleration with holed targets, J. Plasma Phys. **86**, 905860304 (2020).

[75] G. Cantono, A. Permogorov, J. Ferri, E. Smetanina, A. Dmitriev, A. Persson, T. Fülöp, C.-G. Wahlström, Laser-driven proton acceleration from ultrathin foils with nanoholes, Sci. Rep. **11**, 5006 (2021).

[76] Z. Gong, S. S. Bulanov, T. Toncian, and A. V. Arefiev, Energy-chirp compensation of laser-driven ion beams enabled by structured targets, arXiv:1807.07629.

[77] D. J. Stark, T. Toncian, and A. V. Arefiev, Enhanced Multi-MeV Photon Emission by a Laser-Driven Electron Beam in a Self-Generated Magnetic Field, Phys. Rev. Lett. **116**, 185003 (2016).

[78] O. Jansen, T. Wang, D. J. Stark, E. d'Humières, T. Toncian, and A. V. Arefiev, Leveraging extreme laser-driven magnetic fields for gamma-ray generation and pair production, Plasma Phys. Control. Fusion **60**, 054006 (2018).

[79] Y. He, T. G. Blackburn, T. Toncian, A. V. Arefiev, Dominance of $\gamma$-$\gamma$ electron-positron pair creation in a plasma driven by high-intensity lasers, Commun. Phys. **4**, 139 (2021).

[80] H. G. Rinderknecht, T. Wang, A. Laso Garcia, G. Bruhaug, M. S. Wei, H. J. Quevedo, T. Ditmire, J. Williams, A. Haid, D. Doria *et al.*, Relativistically transparent magnetic filaments: Scaling laws, initial results and prospects for strong-field QED studies, New J. Phys. **23**, 095009 (2021).

[81] D. Y. Li, T. Yang, M. J. Wu, H. Cheng, Y. Z. Li, Y. D. Xia, Y. Yan, Y. X. Geng, Y. Y. Zhao, C. Lin *et al.*, Manipulation of laser-accelerated proton beam spatial distribution by laser machined microstructure targets, Phys. Plasmas **28**, 113101 (2021).

[82] A. I. Akhiezer and R. V. Polovin, Theory of wave motion of an electron plasma, Sov Phys.-JETP **3**, 696 (1956).

[83] S. V. Bulanov, T. Zh. Esirkepov, M. Kando, J. K. Koga, S. S. Bulanov, Lorentz-Abraham-Dirac vs Landau-Lifshitz radiation friction force in the ultrarelativistic electron interaction with electromagnetic wave (exact solutions), Phys. Rev. E **84**, 056605 (2011).

[84] C. P. Ridgers, J. G. Kirk, R. Duclous, T. G. Blackburn, C. S. Brady, K. Bennett, T. D. Arber, and A. R. Bell, Modelling gamma-ray photon emission and pair production in high-intensity laser–matter interactions, J. Comput. Phys. **260**, 273 (2014).

[85] T. D. Arber, K. Bennett, C. S. Brady, A. Lawrence-Douglas, M. G. Ramsay, N. J. Sircombe, P. Gillies, R. G. Evans, H. Schmitz, A. R. Bell, and C. P. Ridgers, Contemporary particle-in-cell approach to laserplasma modelling, Plasma Phys. Control. Fusion **57**, 113001 (2015).

[86] FLASH Code, https://flash.rochester.edu/site/index.shtml.

[87] P. Tzeferacos, M. Fatenejad, N. Flocke, C. Graziani, G. Gregori, D. Q. Lamb, D. Lee, J. Meinecke, A. Scopatz, K. Weide, FLASH MHD simulations of experiments that study shock-generated magnetic fields, High Energy Density Phys. **17**, 24 (2015).

[88] V. B. Pathak, S. K. Lee, K. H. Pae, C. I. Hojbota, C. M. Kim, and C. H. Nam, Strong field physics pursued with petawatt lasers, AAPPS Bull. **31**, 4 (2021).

[89] S. P. D. Mangles, B. R. Walton, M. Tzoufras, Z. Najmudin, R. J. Clarke, A. E. Dangor, R. G. Evans, S. Fritzler, A. Gopal, C. Hernandez-Gomez *et al.*, Electron Acceleration in Cavitated Channels Formed by a Petawatt Laser in Low-Density Plasma, Phys. Rev. Lett. **94**, 245001 (2005).

[90] Z. Gong, F. Mackenroth, T. Wang, X. Q. Yan, T. Toncian, A. V. Arefiev, Direct laser acceleration of electrons assisted by strong laser-driven azimuthal plasma magnetic fields, Phys. Rev. E **102**, 013206 (2020).

[91] M. Jirka, M. Vranic, T. Grismayer, L. O. Silva, Scaling laws for direct laser acceleration in a radiation-reaction dominated regime, New J. Phys. **22**, 083058 (2020).

[92] N. Naumova, J. Koga, K. Nakajima, T. Tajima, T. Zh. Esirkepov, S. V. Bulanov, F. Pegoraro, Polarization, hosing and long time evolution of relativistic laser pulses, Phys. Plasmas **8**, 4149 (2001).

[93] J. W. Yoon, Y. G. Kim, I. W. Choi, J. H. Sung, H. W. Lee, S. K. Lee, and C. H. Nam, Realization of laser intensity over $10^{23}\mathrm{W/cm}^2$, Optica **8**, 630 (2021).

[94] S. Weber, S. Bechet, S. Borneis, L. Brabec, M. Bučka, E. Chacon-Golcher, M. Ciappina, M. DeMarco, A. Fajstavr, K. Falk *et al.*, P3: An installation for high-energy density plasma physics and ultra-high intensity laser–matter interaction at ELI-Beamlines, Matter Radiat. Extremes **2**, 149 (2017).

[95] S. Borneis, T. Laštovicka, M. Sokol, T.-M. Jeong, F. Condamine, O. Renner, V. Tikhonchuk, H. Bohlin1, A. Fajstavr1, J.-C. Hernandez *et al.*, Design, installation and commissioning of the ELI-Beamlines high-power, high-repetition rate HAPLS laser beam transport system to P3, High Power Laser Sci. Eng. **9**, e30 (2021).

[96] W. P. Leemans, J. Daniels, A. Deshmukh, A. J. Gonsalves, A. Magana, H. S. Mao, D. E. Mittelberger, K. Nakamura, J. R. Riley, D. Syversrud *et al.*, BELLA laser and operations, *Proceedings of PAC2013* (2013)

[97] J. Babaei, L. A. Gizzi, P. Londrillo, S. Mirzanejad, T. Rovelli, S. Sinigardi, and G. Turchetti, Rise time of proton cut-off energy in 2D and 3D PIC simulations, Phys. Plasmas **24**, 043106 (2017).

[98] K. D. Xiao, C. T. Zhou, K. Jiang, Y. C. Yang, R. Li, H. Zhang, B. Qiao, T. W. Huang, J. M. Cao, T. X. Cai *et al.*, Multidimensional effects on proton acceleration using high-power intense laser pulses, Phys. Plasmas **25**, 023103 (2018)

[99] J. Psikal, Laser-driven ion acceleration from near-critical Gaussian plasma density profile, Plasma Phys. Control. Fusion **63**, 064002 (2021).

[100] T. Wang, D. Blackman, K. Chen, A. Arefiev, Effects of simulation dimensionality on laser-driven electron acceleration and photon emission in hollow microchannel targets, Phys. Rev. E **104**, 045206 (2021)

[101] J. J. Honrubia, J. C. Fernández, M. Temporal, B. M. Hegelich, and J. Meyer-ter-Vehn, Fast ignition of inertial fusion targets by laser-driven carbon beams, Phys. Plasmas **16**, 102701 (2009).

[102] M. Murakami, J. J. Honrubia, K. Weichman, A. V. Arefiev, S. V. Bulanov, Generation of megatesla magnetic fields by intense-laser-driven microtube implosions, Sci. Rep. **10**, 16653 (2020).

[103] D. J. Stark, L. Yin, B. J. Albright, W. Nystrom, R. Bird, A detailed examination of laser-ion acceleration mechanisms in the relativistic transparency regime using tracers, Phys. Plasmas **25**, 043114 (2018).

[104] L. Yin, B. J. Albright, D. Jung, R. C. Shah, S. Palaniyappan, K. J. Bowers, A. Henig, J. C. Fernandez, and B. M. Hegelich, Break-out afterburner ion acceleration in the longer laser pulse length regime, Phys. Plasmas **18**, 063103 (2011).

[105] D. Ursescu, G. Chériaux, P. Audebert, M. Kalashnikov, T. Toncian, M. Cherchez, M. Kaluza, G. Paulus, G. Priebe, R. Dabu *et al.*, Laser beam delivery at ELI-NP, Rom. Rep. Phys. **68**, S11 (2016).

[106] H. Kiriyama, A. S. Pirozhkov, M. Nishiuchi, Y. Fukuda, K. Ogura, A. Sagisaka, Y. Miyasaka, M. Mori, H. Sakaki, N. P. Dover *et al.*, High contrast high intensity repetitive petawatt laser, Opt. Lett. **43**, 2595 (2018).